PHYSICAL REVIEW D **100,** 035016 (2019)

LHC constraints on a $(B-L)_3$ gauge boson

Fatemeh Elahi[1] and Adam Martin[2]
[1]*School of Particles and Accelerators, Institute for Research in Fundamental Sciences IPM,*
P.O. Box 19395-5531, Tehran, Iran
[2]*Department of Physics, 225 Nieuwland Science Hall, University of Notre Dame,*
Notre Dame, Indiana 46556, USA

(Received 3 June 2019; published 19 August 2019)

In this paper, we explore the constraints that the LHC can place on a massive gauge boson X that predominantly couples to the third generation of fermions. Such a gauge boson arises in scenarios where the $B-L$ of the third generation is gauged. We focus on the mass range $10 \leq m_X \lesssim 2m_W$, where current constraints are lacking, and develop a dedicated search strategy. For this mass range, we show that (semi)-leptonic $b^+b^-\tau^+\tau^-$ is the optimal channel to look for the X at the LHC. The QCD production of b quarks, combined with the cleanliness of the leptons coming from the decay of the τ, allows us to detect the X gauge boson with couplings of $g_X \sim (0.005\text{–}0.01)$, for $m_X < 50$ GeV, and a coupling of $O(0.1)$ for a heavier X gauge boson with 100 fb^{-1} of integrated luminosity. This is about a factor of 2–10 improvement over previous constraints coming from the decay of $\Upsilon \to \tau^+\tau^-$. Extrapolating to the full HL-LHC luminosity of 3000 fb^{-1}, the bounds on g_X can be enhanced by another factor of $\sqrt{2}$ for $m_X < 50$ GeV.

DOI: 10.1103/PhysRevD.100.035016

I. INTRODUCTION

Even though numerous experimental measurements attest to the validity of the Standard Model (SM), some enigmatic observations such as dark matter and neutrino masses compel us to look for new physics (NP) beyond the SM. Many NP models propose augmenting the SM gauge groups by a new gauge symmetry, with $U(1)$ being a popular choice. On the other hand, it is well known that the SM Lagrangian respects some global $U(1)$ symmetries that are not demanded beforehand. Some of these so-called accidental symmetries are anomaly free and can be gauged, either within the SM alone or with minimal extension [1–5]. Given that nature already approves of the SM, it is worthwhile to explore extending the SM using its own suggested symmetries.

Among the possible symmetries, new interactions that involve electrons or the first two generations of quarks are severely constrained in various collider searches [6–11] and low-energy experiments [12–15]. The $U(1)_{L_\mu-L_\tau}$ symmetry—the difference between muon and tau number—has also received a lot of attention in recent years [3,16–30], and much of its parameter space is already being probed. That leaves us with new gauge bosons that interact predominantly with the third generation of fermions. One such possibility is $U(1)^{(3)}_{B-L}$, the difference between baryon number and lepton number of the third generation, which is anomaly free and guageable provided we augment the SM by a right-handed neutrino [31–34].

The $U(1)^{(3)}_{B-L}$ extension of the SM was discussed in Ref. [32] to explain the flavor alignment of the third generation of quarks—the empirical observations that the mixings of the third generation of quarks with the other two generations are very small. Distinguishing the third generation by assigning it new quantum numbers under an additional symmetry prohibits the mixing with the third generation of quarks[1] and thus justifies its flavor alignment. Of course, the symmetry needs to be broken at some scale to allow small, yet nonzero mixing between the generations [35].

To achieve nonzero mixing between the generations at low scales, the $U(1)^{(3)}_{B-L}$ symmetry needs to be spontaneously broken by a scalar ϕ that is charged under

---

[1] By distinguishing the third generation of quarks under the new symmetry, $U(1)^{(3)}_{B-L}$, the Lagrangian terms $y^u_{ij}\bar{Q}_i\tilde{H}u_j + y^d_{ij}\bar{Q}_iHd_j$, with $ij = 13, 23, 31, 32$, are forbidden. Therefore, as long as this symmetry is preserved, the physical top and bottom (in their mass basis) are completely aligned with their weak interaction basis. However, empirical observations show that the mixing is not exactly zero. To generate nonzero mixing, $U(1)^{(3)}_{B-L}$ must be spontaneously broken by another scalar ϕ at a scale below the electroweak scale.

$U(1)^{(3)}_{B-L} \times \mathcal{G}_{\rm SM}$ and acquires a vacuum expectation value (vev). For certain charge assignments and coupling structure, it is possible to generate a realistic Cabbibo–Kobayashi–Maskawa (CKM) matrix while relegating all tree-level flavor-changing neutral currents (FCNCs) to the up-quark sector [32] (see also the Appendix C). The up-sector FCNCs are suppressed by powers of CKM elements; however, they—along with the down-sector FCNCs they generate at loop level—are constrained by multiple low-energy experiments. The constraints from experiments such as *BABAR* [12], E949 [36,37], BESIII [38], and CHARM-II [39] are severe but peter out once $m_X \gtrsim 5\,\text{GeV}$. Furthermore, the direct coupling of X with the third generation of fermions can also contribute to the decay of $\Upsilon \to \tau\tau$, which constrains the available parameter space for X near $m_X \sim m_\Upsilon \simeq 10$ GeV [40]; however, the contribution of off-shell X to Υ decay dies off rapidly as we move away from m_Υ.

The m_X window less than about 10 GeV is only loosely constrained and is therefore the focus of this study. In practice, we impose an upper limit of $m_X < 2m_W$, as the interaction of X with W gauge bosons is closely tied to the mixing angle between Higgs and the $U(1)^{(3)}_{B-L}$ breaking scalars ϕ and thus introduces multiple additional parameters; X in this range could conceivably be constrained by LHC resonant diboson searches such as Refs. [41–45]. For even larger $m_X > 2m_t$, X phenomenology is driven by decays to top pairs. In this sense, X phenomenology can be mapped into $Z' \to t\bar{t}$ searches, which have been studied extensively [46–62].

Having selected the X mass window we are interested in, the next step is to determine the optimal LHC X production mode and decay channel. As X has suppressed couplings to first and second generation fermions, we either have to rely on the b parton distribution function (PDF) (for $pp \to X$) or to produce the X in association with third generation fermions, e.g., $pp \to \bar{f}fX$ where $f = t/b/\tau/\nu_\tau$. The PDF of the b quark is small; therefore, we focus on associated production.[2] The production of colored objects at the LHC is significantly larger than leptons; therefore, we will concentrate on the scenario where X is produced in association with a pair of b quarks. Associated production of X with top quarks is also an option but suffers in rate due to the increased energy requirement as well as in reconstruction complexity, so we do not consider it here.

Turning to X decay, if X decays to a pair of b quarks, we have a four-b final state, which makes QCD backgrounds overwhelming and introduces a combinatorics problem. Among the leptonic decays of X, τs are more preferable because they give more handles for kinematic variables. Thereby, we settle on $pp \to b\bar{b}X \to b\bar{b}\tau^+\tau^-$.

One may think that further focusing the search on the Z resonance contribution is a useful way to suppress backgrounds, as done in Ref. [29] for the case of $U(1)_{L_\mu - L_\tau}$ gauge bosons in $pp \to 4\mu$. However, the poorer energy resolution for jets (as compared to muons in Ref. [29]) and the inevitable missing energy from neutrinos in tau decay hamper this technique, and we find it is more beneficial to focus on QCD-produced $b\bar{b}$ pairs that emit an $X \to \tau^+\tau^-$.

The channel $b\bar{b}\tau^+\tau^-$ has already attracted some attention at the LHC in the search for the third generation leptoquarks [63,64] and di-Higgs searches [65–67]. However, due to their particular optimized cuts, these analyses will have limited to no sensitivity to X in our mass range of interest. More specifically:

(i) the search for the third generation leptoquarks [63,64] is ineffective because they impose $m_{\tau b} > 250$ GeV, whereas we find that our signal prefers $m_{\tau b} < 150$ GeV for $m_X \le 2m_W$.

(ii) the CMS di-Higgs search [65] considers $b\bar{b}\tau^+\tau^-$ in the mass window 400 GeV $< m_{bb\tau\tau} <$ 700 GeV. In our signal, however, the production of $b\bar{b}X$ is maximum at threshold, which means even for $m_X = 2m_W$ we expect most of our events to lie in the $m_{bb\tau\tau} < 350$ GeV region.

(iii) the results of other CMS di-Higgs searches [66,67] are not easily recastable because they use a boosted decision tree.

Given the lack of constraints from the current LHC searches or any other experiments, in the following sections, we develop a LHC search strategy for $U(1)^{(3)}_{B-L}$ gauge bosons, 10 GeV $\le m_X \le 2m_W$, using the $b\bar{b}\tau^+\tau^-$ final state. We will assume throughout that X is short lived and therefore focus on prompt signals. Long-lived X, leading to displaced vertices at the LHC, may be interesting to study but likely require extending the setup in some way.[3] For the case of fully hadronic $b\bar{b}\tau^+\tau^-$ (prompt), the QCD backgrounds are overwhelming. Therefore, we will narrow our attention to semileptonic and fully leptonic decays of τs. Despite the large SM backgrounds (e.g., $t\bar{t} \to b\bar{b}W^\pm W^\pm \to b\bar{b}\tau^+\tau^- + \not{E}_T$), we show that the LHC-13 TeV, with the currently luminosity, can significantly improve the bounds on the $U(1)^{(3)}_{B-L}$ gauge coupling g_X.

The organization of the rest of the paper is as follows. In the upcoming section (Sec. II), we introduce the model, including the free parameters we will consider for the phenomenology of X gauge boson at the LHC. Next, in Sec. III, we explore the LHC power in improving the bounds using simple kinematic variables—both for $m_X < m_Z$ (Sec. III A) and for slightly heavier $m_X \gtrsim m_Z$ (Sec. III B). Finally, some concluding remarks are presented in Sec. IV.

---

[2] While they are smaller, we do include processes initiated by b PDFs in all our analyses.

[3] In the current setup, the X lifetime and production rate are governed by the same coupling, so one cannot make the particle long lived without killing the production rate.

II. $U(1)^{(3)}_{B-L}$ MODEL

We study a model where the SM gauge symmetries are extended to include $U(1)^{(3)}_{B-L}$ symmetry—the difference between the baryon number and the lepton number of the third generation. This symmetry is anomaly free, provided that we include a right-handed tau neutrino ν_{3R} to the SM. The charge assignments of the fermions are (Q_{3L}, u_{3R}, d_{3R}): 1/3 and $(\ell_{3L}, e_{eR}, \nu_{3R})$: -1, with all first and second generation fermions inert.

From various observations, we know the exact $U(1)^{(3)}_{B-L}$ symmetry is not realized in nature at low scales and thus must be broken. The simplest mechanism to spontaneously break $U(1)^{(3)}_{B-L}$ is to add some scalars charged under $U(1)^{(3)}_{B-L}$ symmetry that acquire vevs. To make the model phenomenologically viable, we actually have to introduce two $U(1)_{B-L}$ charged scalars: an SM singlet s with $U(1)_{B-L}$ charge $+1/3$ and ϕ, an SM $SU(2)_W$ doublet with hypercharge $+1/2$ (identical SM shares as the Higgs) and $U(1)_{B-L}$ charge $+1/3$ [32]. The table of particles charged under $U(1)^{(3)}_{B-L}$ is shown in Table I. The ϕ field is needed to connect first and second generation quarks to the third generation quarks via renormalizable interactions, while the additional source of $U(1)^{(3)}_{B-L}$ breaking from the s field allows us to decouple the mass of the $U(1)^{(3)}_{B-L}$ gauge boson X from the electroweak breaking scale. Note that Yukawa terms involving only third generation fields involve the Higgs, not s or ϕ, and that renormalizable intergeneration interactions involving the third generation between leptons are forbidden by the $U(1)^{(3)}_{B-L}$ charge assignment. Neutrino masses can be accommodated via higher-dimensional operators or via further extensions of the model by vectorlike matter [32]. The modification to the Lagrangian can be found in Appendix B.

In this paper, we are interested in the phenomenology of the X gauge boson. The X gauge boson appears in the covariant derivative of the third generation fermions, indicating a tree-level interaction of X with third generation of fermions in the interaction basis. Another place X appears is the covariant derivative of scalars (s and ϕ), which not only results in X acquiring a mass (once $\langle\phi\rangle$, $\langle s\rangle \neq 0$) but also leads to tree-level interactions of X with scalars. Furthermore, because ϕ is charged under both $SU(2)_{\mathrm{W}} \times U(1)_{\mathrm{Y}}$ and $U(1)^{(3)}_{B-L}$, its kinetic term induces a mixing with X and Z gauge boson with an angle [32]

$$s_X \equiv \frac{2}{3}\frac{g_X}{\sqrt{g^2+g'^2}}\frac{v_\phi^2}{v^2}, \tag{1}$$

where (v_ϕ) represents ϕ vev and $v = \sqrt{v_\phi^2 + v_h^2} = 246\,\mathrm{GeV}$, with v_h being the Higgs vev. Therefore, in the mass basis, the (mass eigenstate) X boson interacts with Z current with a coupling proportional to s_X, while the (mass eigenstate) Z boson interactions will be modified by an amount proportional to s_X.

TABLE I. Scalar and fermion fields charged under the $U(1)^{(3)}_{B-L}$ gauge symmetry.

	$SU(3)_c \times SU(2)_{\mathrm{W}} \times U(1)_{\mathrm{Y}}$	$U(1)^{(3)}_{B-L}$
ϕ	$(\mathbf{1}, \mathbf{2}, 1/2)$	1/3
s	$(\mathbf{1}, \mathbf{1}, 0)$	1/3
h	$(\mathbf{1}, \mathbf{2}, 1/2)$	0
Q_{3L}	$(\mathbf{3}, \mathbf{2}, -1/6)$	1/3
t_R	$(\mathbf{3}, \mathbf{1}, 2/3)$	1/3
b_R	$(\mathbf{3}, \mathbf{1}, -1/3)$	1/3
L_{3L}	$(\mathbf{1}, \mathbf{2}, -1/2)$	−1
τ_R	$(\mathbf{1}, \mathbf{1}, -1)$	−1
$\nu_{\tau R}$	$(\mathbf{1}, \mathbf{1}, 0)$	−1

In addition to X, the model contains several new scalars (from ϕ, s) and a right-handed neutrino. For simplicity, and following Ref. [32], we assume that these states are all heavier than $m_X/2$, so they play no role in our analysis.

The relevant model parameters to study X_μ phenomenology are the X mass (m_X), the $U(1)^{(3)}_{B-L}$ gauge coupling (g_X), and the rotation angle between Z and X (s_X). Rather than use s_X, we find it more convenient to work with $\tan\beta = v_h/v_\phi$. In terms of these parameters,

$$m_X^2 = \frac{1}{9}g_X^2\left(\frac{v_\phi^2 v_h^2}{v^2} + v_s^2\right) = \frac{1}{9}g_X^2\left(v^2\frac{\tan^2\beta}{(1+\tan^2\beta)^2} + v_s^2\right). \tag{2}$$

Notice that the presence of v_s means m_X is not tied to the electroweak scale and can, in principle, be large.

In the gauge interaction basis, the interaction between fermions and the (mass eigenstate) X gauge boson has the form $c_\alpha \bar{f}_\alpha \gamma^\mu f_\alpha X^\mu$, with

$$\begin{aligned} c_\alpha &= g_X q_\alpha^X + s_X\sqrt{g^2+g'^2}\,q_\alpha^Z \\ &= g_X\left[q_\alpha^X + \frac{2}{3}q_\alpha^Z(1+\tan\beta^2)^{-1}\right]. \end{aligned} \tag{3}$$

Here, q_α^X and $q_\alpha^Z = I_3^\alpha - s_w^2 q_\alpha$ are, respectively, the X and Z charge of fermion α; q_α is the electric charge; s_w is the $\sin\theta_{\mathrm{weak}}$; and I_3^α is the W_μ^3 generator.[4] The translation of this interaction to the fermion mass basis induces

---

[4] More explicitly, here are some of the most important couplings of X: $c_\tau = g_X[-1 + \frac{2}{3}((-\frac{1}{2} + 2s_w^2) - \frac{1}{2}\gamma_5)(1+\tan^2\beta)^{-1}]$, $c_b = g_X[\frac{1}{3} + \frac{2}{3}((-\frac{1}{2} + \frac{2}{3}s_w^2) - \frac{1}{2}\gamma_5)(1+\tan^2\beta)^{-1}]$, $c_{v_\tau} = g_X[-1 + \frac{2}{3}(\frac{1}{2} + \frac{1}{2}\gamma_5)(1+\tan^2\beta)^{-1}]$.

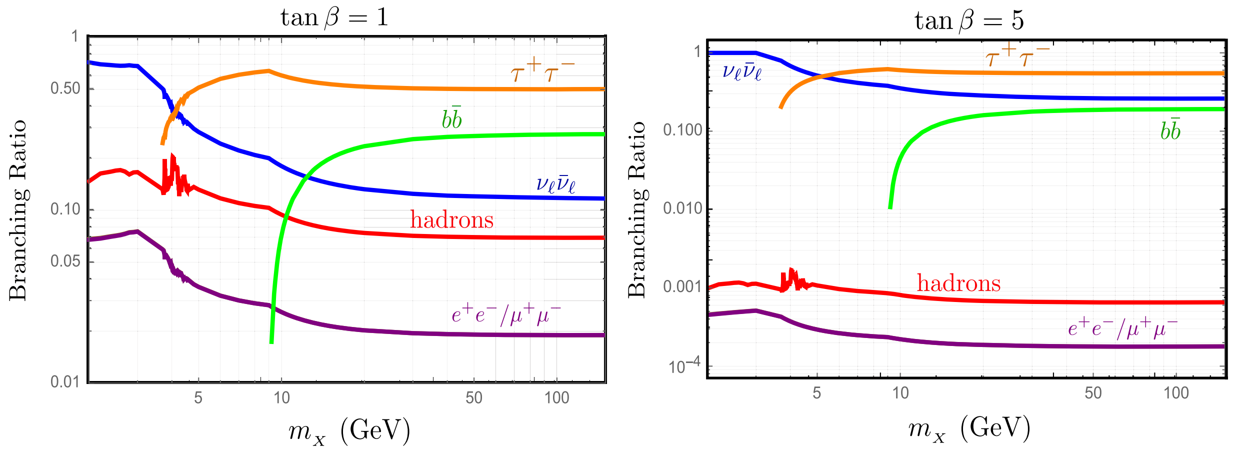

FIG. 1. The branching ratio of X to various final states for $\tan\beta = 1$ (left) and $\tan\beta = 5$ (right), with the assumption that the new scalars and the sterile neutrino are heavier than $m_X/2$. The branching ratio differs significantly depending on the value of $\tan\beta$. The highest branching ratio in the heavy mass region is to $\tau^+\tau^-$, due to a combination of large q_X and large electromagnetic charge.

flavor-changing interactions among left-handed up-type quarks and is shown in detail in Appendix C.

An important property of X for our study is how it decays to various SM states. Due to $X - Z$ mixing, the branching ratio of X strongly depends on the value of $\tan\beta$. For small $\tan\beta$, the coupling of X to the Z current is important, while for large $\tan\beta$, X predominantly decays to third generation fermions. The branching ratio of X to various SM final states for $\tan\beta = 1$ and $\tan\beta = 5$ is shown in Fig. 1.[5] In this figure, we derived the branching ratio of X to hadrons using Ref. [68], and we have assumed the new scalars and the sterile neutrino are heavier than $m_X/2$. We can see that the branching ratio of X to a pair of τs dominates for $m_X \gtrsim 5$ GeV (and up to $m_X \sim 2m_W$). This channel dominates because of the relatively large values of q_τ^X and q_τ^Z compared to other third generation fermions.

Having defined the model, we now move on to its LHC signatures. As mentioned earlier, our focus is on $m_X > 10$ GeV where low-energy constraints are absent. For $m_X > 10$ GeV, the only non-LHC bounds are from $\Upsilon \to \tau^+\tau^-$ and the modification of the oblique parameters. The contribution of off-shell X to Υ decay dies off rapidly as $1/m_X^2$, and the constraints coming from oblique parameters become very mild for $\tan\beta > 2$.

III. LHC CONSTRAINTS

The main advantage of the LHC is that it can produce the X gauge boson on shell. This fact is crucial because amplitudes containing off-shell X are suppressed by two powers of g_X—one at the production vertex and another at its destruction. On-shell exchange, on the other hand, comes with only one factor of g_X at the X production vertex (amplitude level) as the decay portion contributes some $O(1)$ branching ratio factor.

The chief way to produce an on-shell X at the LHC is in associated production with a pair of b jets,[6] $pp \to b\bar{b}X$. In such processes, we can benefit from the large QCD production of bs as well as the sizable coupling of X with b quarks. The X boson can decay in many ways; however, we will focus here on $pp \to b\bar{b}X \to b\bar{b}\tau^+\tau^-$. This choice is motivated by the large $\mathrm{Br}(X \to \tau^+\tau^-)$; however, there are some other important benefits:

(i) There is a large number of observables to help signal background discrimination, in contrast to $b\bar{b} + \not{E}_T$ production.

(ii) There are no combinatorics issues, as opposed to the $\bar{b}b\bar{b}b$ final state.

Because τs are not stable at the LHC, the search mode has to be further defined in terms of the $\tau^+\tau^-$ final decay products. While there exist several options, we find that requiring at least one of the τs to decay leptonically is necessary to suppress the (otherwise enormous) QCD background. To decide between semileptonic τs or fully leptonic ones, let us turn our attention to potential triggers.[7] As leptons are relatively clean objects at the LHC, they have softer trigger cuts, and the presence of multiple leptons softens the requirement on each lepton further. As an example, the single lepton trigger at CMS [69,70]

---

[5] There is a constraint on the value of $\tan\beta$ coming from Higgs coupling measurements, roughly between $1 \leq \tan\beta \leq 30$. The exact range depends on the scalar h, ϕ, s spectrum, the details of which we ignore here; therefore, we will work with this approximate range.

[6] The cross section of $pp \to bbX$ is roughly 2 orders of magnitude greater than $pp \to X$ for $m_X \sim 10$ GeV, but the difference decreases as we increase the mass. For $m_X \sim 100$ GeV, the difference between the cross sections of $pp \to bbX$ and $pp \to X$ is about 1 order of magnitude.

[7] As we will show in the subsequent sections, the $\not{E}_T$ distribution in the signal favors lower values. Therefore, a $\not{E}_T$ trigger is also not ideal for our study.

requires $p_T(\ell) > 23(20)$ GeV if the lepton is an electron (muon), and the CMS dilepton trigger [69,70] requires $p_T(\ell_1) > 17$ GeV and $p_T(\ell_2) > 12(8)$ GeV with the second leading lepton being an electron (muon).[8] Production of $b\bar{b}X$ is dominated near threshold (rather than with boosted X); hence, the leptons coming from a light X are expected to have small p_T. Therefore, for low m_X, the fully leptonic τs is the better option since the softer thresholds in the dilepton trigger will accept more signal. For high m_X, the leptons from X decay are significantly energetic to be picked up efficiently by the single lepton trigger. This makes the semileptonic mode viable, and its larger branching fraction (compared to dileptonic taus) partially compensates for the drop in the signal cross section as m_X increases.

As the optimal $b\bar{b}\tau^+\tau^-$ final state depends on m_X, we divide our analysis into two sections. In the following section (Sec. III A), we study X gauge bosons with $m_X < m_Z$ using the $b\bar{b}\ell^+\ell^-\not{E}_T$ final state. Then, in Sec. III B, we use the $b\bar{b}\ell j\not{E}_T$ final state to explore heavier X gauge bosons, $m_X \sim [m_Z, 2m_W)$. To thoroughly study the LHC detection prospects, we generated a Universal FeynRules Output model [73] using FEYNRULES [74]. We then fed the model to MADGRAPH-AMC@NLO [75,76] for all simulations,[9] including the calculation of X total width for a given coupling (g_X and s_X). We used PYTHIA8.2 [77] for hadronization, showering, and τ decay and Delphes [78] with default cards for detector smearing, flavor tagging, and jet reconstruction.

A. Light X: $m_X < m_Z$

As discussed above, for $m_X < m_Z$, the final state we are interested in extracting is $b\bar{b}\ell^+\ell^-\not{E}_T$. The main contribution to the signal comes from $pp \to b\bar{b}X$ with $X \to \tau^+\tau^-$ (specifically, the process $pp \to \tau^+\tau^- X$ followed by $X \to b\bar{b}$ only contributes to the signal at subpercent level); Fig. 2 shows some of the signal processes. Because X is predominantly produced on shell, the signal has little interference with the SM backgrounds. Therefore, to a good approximation, the cross section can be expressed as

$$\sigma(pp \to b\bar{b}\tau^+\tau^-)_{\text{Signal}} \sim c_b(g_X, \tan\beta)^2 \times f(m_X, s) \times \text{Br}(X \to \tau^+\tau^-)_{\tan\beta}, \tag{4}$$

where $c_b(g_X, \tan\beta)$ is the coupling of X with b quarks. The subscript $\tan\beta$ in Eq. (4) indicates that the branching ratio

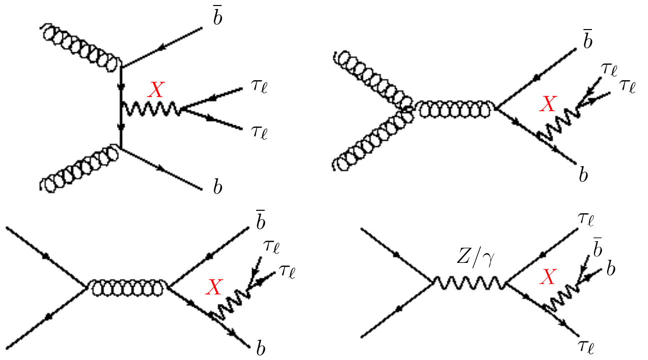

FIG. 2. The signal Feynman diagrams corresponding to the production of $b\bar{b}\ell^+\ell^-\not{E}_T$ final state.

of X depends on $\tan\beta$. Technically, the branching ratio depends on m_X as well; however, for the mass range of $2m_b \le m_X < 2m_W$, the branching ratios are constant with respect to m_X. The remaining part of the cross section, $f(m_X, s)$, governs the kinematics and is a function of m_X and collider energy s only. In our simulations, we generated events for $m_X = 10$, 20, 30, 50, and 80 GeV and fixed $g_X = 0.02$ and $\tan\beta = 5$. However, as $c_b(g_X, \tan\beta) \times \text{Br}(X \to \tau^+\tau^-)_{\tan\beta}$ do not play a noticeable role in the kinematic distributions (which govern signal acceptances), the LHC sensitivity at one g_X, $\tan\beta$ value can be extended to other g_X, $\tan\beta$ values simply by rescaling,

$$\sigma^{\text{New}}_{\text{Signal}} \sim \sigma^{\text{Old}}_{\text{Signal}} \left(\frac{c_b(g^n_X, \tan\beta^n)}{c_b(g^o_X, \tan\beta^o)}\right)^2 \times \frac{\text{Br}(X \to \tau^+\tau^-)_{\tan\beta^n}}{\text{Br}(X \to \tau^+\tau^-)_{\tan\beta^o}}, \tag{5}$$

where the indices n and o refer to new and old, respectively.

There are a number of SM processes that give rise to the $b\bar{b}\ell^+\ell^-\not{E}_T$ final state, namely,

$$\begin{aligned} &1)\ pp \to b\bar{b}V_{\ell+\tau_\ell}V_{\ell+\tau_\ell}: \begin{cases} b\bar{b}W^+_{\ell+\tau_\ell}W^-_{\ell+\tau_\ell} \\ b\bar{b}(Z/\gamma^\star)_{\ell+\tau_\ell}Z_\nu \end{cases} \\ &2)\ pp \to b\bar{b}\tau^+_\ell\tau^-_\ell \\ &3)\ pp \to b\bar{b}\ell^+\ell^-, \end{aligned} \tag{6}$$

where $\ell = e, \mu$ and $(W/Z)_{\ell+\tau}$ refers to all possible charged leptonic decays of W/Z. Similarly, τ_ℓ refers to the decay of τ to lighter leptons. The main difference between these three backgrounds is the number of neutrinos. The first background has two or six neutrinos, depending on whether the gauge bosons decay to ℓ or τ_ℓ, respectively; the second background has four; and the third does not have any neutrinos. However, due to pileup, jet mismeasurement, and the leptonic decays of a charged B mesons in the b jets, a net $\not{E}_T$ can be generated, making the last background worth mentioning.

---

[8] The ATLAS numbers trigger cuts are similar: a single lepton requires the $p_T(\ell) > 26$ GeV [71,72], while the dilepton trigger requires $p_T(\ell) > 17$ GeV, on both of the leading leptons [72].

[9] We used the NN23LO1 parton distribution functions for all event samples, with the factorization scale and renormalization scale set to their default values, $\hat{s}$.

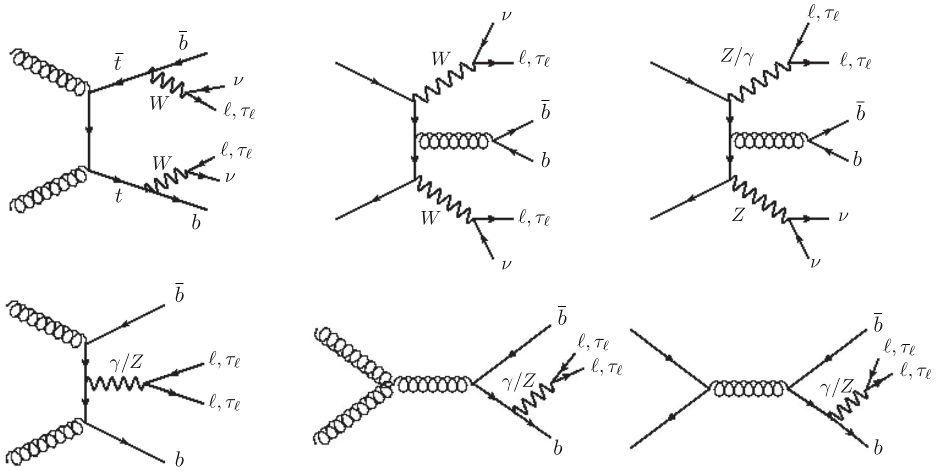

FIG. 3. The SM backgrounds to $b\bar{b}\ell^+\ell^- + \not{E}_T$ production at the LHC. In these diagrams, $\ell = \mu$, e, and τ_ℓ refers to a τ that decays leptonically. The first line in the Feynman diagrams corresponds to the first mentioned background in Eq. (6). The second and third backgrounds in Eq. (6) are shown in the second line of these Feynman diagrams, where the gauge bosons decay to τ_ℓ and ℓ, respectively.

A few of the important Feynman diagrams for the SM production of $b\bar{b}\ell^+\ell^-\not{E}_T$ are shown in Fig. 3. The largest irreducible background comes from $pp \to t\bar{t} \to b\bar{b}W^+W^-$, as it is purely a QCD process with $\mathrm{Br}(t \to bW) \simeq 1$. Other (continuum) processes contributing to the first background in Eq. (6) do not have a large rate. The second background, $b\bar{b}\tau_\ell^+\tau_\ell^-$, is very similar to the signal, where X is replaced with a Z or γ. Technically, the ($pp \to b\bar{b}\tau_\ell^+\tau_\ell^-$) background and the signal can interfere; however, the fact that X are predominantly produced on shell renders the interference is very small.[10] The last background is similar to the second background, but instead of producing a pair of τ leptons, $Z/\gamma \to \ell^+\ell^-$.

We must also include (reducible) backgrounds where a gluon/light flavor jet is misidentified as a b jet. The misidentification rate of a c jets is significantly higher than other light-quark/gluon initiated jets (collectively referred to as j_l). Therefore, we considered charm-jet and light-jet processes separately. To include the impact of misidentifications, we add two versions of all backgrounds in Eq. (6)—one with b jets replaced with c and one with b replaced by j_l. For example, the second background is expanded to include

$$2.)\ pp \to b\bar{b}\tau_\ell^+\tau_\ell^- \Rightarrow \begin{cases} pp \to c\bar{c}\tau_\ell^+\tau_\ell^- \\ pp \to j_l j_l \tau_\ell^+\tau_\ell^-. \end{cases} \tag{7}$$

Other backgrounds induced by lepton misidentification are expected to have very low rates [79–82] and thus are ignored in this study. The Monte Carlo event samples for all processes are simulated at leading order (LO), with the overall rates scaled to next-to-leading order (NLO).[11]

Before studying the kinematic distributions, we impose some preliminary cuts to ensure the events have been triggered upon and that the visible final states are within the fiducial region of the detector. Specifically, we select events that satisfy the following requirements:

(i) Include exactly two isolated opposite-sign leptons (any combination of electrons and muons) with $|\eta| < 2.5$ and separated from each other by $\Delta R > 0.4$. We further require the leptons to satisfy the dilepton trigger; the leading lepton must have $p_T(\ell_1) > 17$ GeV, and the second leading lepton is required to have $p_T(\ell_2) > 12(8)$ GeV if the lepton is an electron (muon).

(ii) Include exactly two jets with $p_T(j) > 30$ GeV, $|\eta| < 2.5$, and separated from each other by $\Delta R > 0.4$. Both jets must be b tagged. We use the b-tagging option in DELPHES [78], which corresponds to roughly a b-tagging efficiency of 60%, with a charm mistagging of 15% and a light jet misidentification rate of 1%.

After these requirements, the largest background is $b\bar{b}V_{\ell+\tau_\ell}V_{\ell+\tau_\ell}$ with a cross section of 1362 fb, followed by $b\bar{b}\ell^+\ell^-$ with a 255 fb cross section, while that of $b\bar{b}\tau^+\tau^-$ is 28 fb. Among the reducible (fake b) backgrounds, $c\bar{c}\ell^+\ell^-$ (20.3 fb), $j_l j_l \ell^+\ell^-$ (8 fb), and $c\bar{c}\tau^+\tau^-$

---

[10] In our simulations, we force X to be on shell. To make sure this shortcut does not significantly influence our results, we tested the effects of off-shell X (and interference) for various values of m_X. In all cases, the difference between on-shell X and the full treatment was negligible.

[11] Using MADGRAPH5-AMC@NLO for a 13 TeV LHC, we find the $\kappa \equiv \sigma_{\mathrm{NLO}}/\sigma_{\mathrm{LO}}$ of the $bbVV$ process is roughly 1.4, for $\kappa_{bb\tau\tau}$ is 1.8, and that of $bb\ell\ell$ is 1.9. For the reducible background where a light flavor/gluon jet is misidentified as a b jet, we assume $\kappa = 2$. The κ of the signal is assumed to be 1.8, due to the similar topology of the signal with the $b\bar{b}\tau^+\tau^-$ background.

TABLE II. The effect of each cut on the signal benchmark with $m_X = 30$ GeV and each of the backgrounds.

Cuts	X_μ	SM backgrounds (fb)			
	(30 GeV, 0.02)	$b\bar{b}\ell^+\ell^-$ $c\bar{c}\ell^+\ell^-$ $j_l j_l \ell^+\ell^-$	$b\bar{b}VV$ $c\bar{c}VV$ $j_l j_l VV$	$b\bar{b}\tau^+\tau^-$ $c\bar{c}\tau^+\tau^-$ $j_l j_l \tau^+\tau^-$	Significance$\vert_{\mathcal{L}=100\ \mathrm{fb}^{-1}}$
Basic selection	8.13	254.3 20.3 8	1362 2 1.8	27.8 2.4 2	0.005
$m_{\ell\ell} < 25$ GeV	7.9	2.6 0.85 0.5	12.44 0.2 0.18	0.16 0.06 0.02	5.77
$\Delta\phi(\ell\ell, \not{E}_T) < 0.53$	6.4	0.3 0.09 0.2	0.44 0.0 0.0	0.13 0.04 0.02	40.0
$14 < \not{E}_T < 50$	5.48	0.09 0.02 0.1	0.3 0.0 0.0	0.07 0.02 0.02	49.0
Efficiencies	67.4%	0.03% 0.01% 0.1%	0.02% 0.0% 0.0%	0.3% 0.8% 1%	

(2.4 fb) are the most significant. The rest of the irreducible backgrounds have cross sections less than or equal to 2 fb (see Table II).

Thankfully, the topology of the dominant background—$b\bar{b}V_{\ell+\tau_\ell}V_{\ell+\tau_\ell}$—is vastly different from the signal, giving us a hope to reduce it further with additional kinematic cuts. One variable that is particularly useful in teasing out the signal is the invariant mass of the leptons. In the signal, we know $m_{\ell\ell} < m_X$, while the invariant mass of the leptons in $b\bar{b}V_{\ell+\tau_\ell}V_{\ell+\tau_\ell}$ has a broad, featureless distribution. Therefore, requiring an upper bound on $m_{\ell\ell}$ can significantly suppress the $b\bar{b}V_{\ell+\tau_\ell}V_{\ell+\tau_\ell}$ background while retaining most of the signal region. A comparison of the $m_{\ell\ell}$ distribution (area normalized) for the background and a signal benchmark, $m_X = 30$ GeV, is shown in the left panel of Fig. 4.

For light m_X, the only background that behaves similarly to the signal is $pp \to \gamma^* \to \tau_\ell^+\tau_\ell^-$, $\ell^+\ell^-$. The cross section

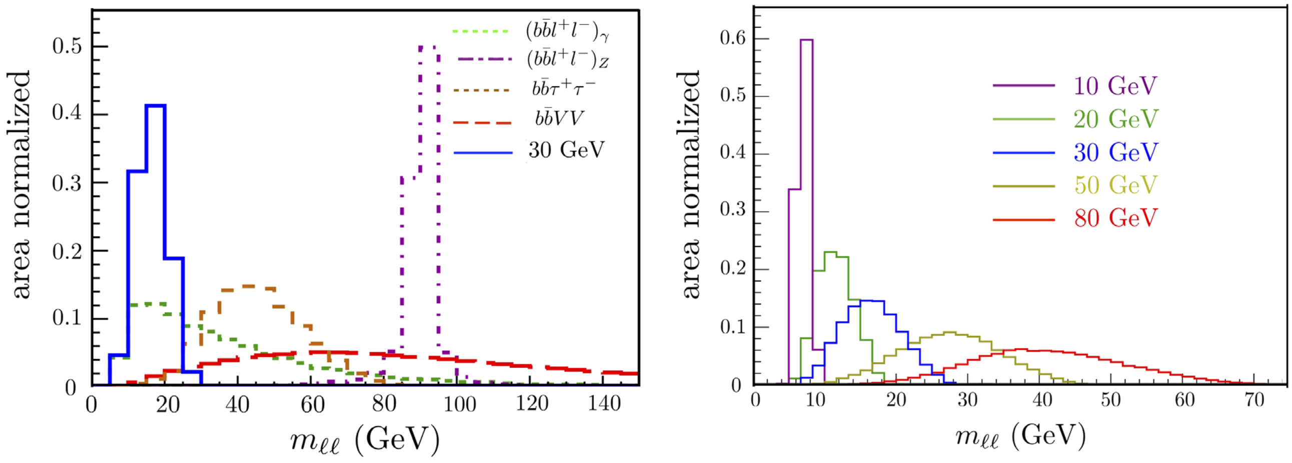

FIG. 4. Left: The area-normalized distribution of invariant mass of the two leptons ($m_{\ell\ell}$) for one of the signal benchmarks $m_X = 30$ GeV, compared with the dominant backgrounds. These distributions are after the basic cuts, and $Z^{(\star)} \to \ell\ell$ and $\gamma^* \to \ell\ell$ have been listed as separate contributions since the interference between them is small. To make the distribution less cluttered, we did not include the reducible backgrounds [Eq. (12)]; however, the distributions of $c\bar{c}\ell^+\ell^-$ and $j_l j_l \ell^+\ell^-$ behave like $b\bar{b}\ell^+\ell^-$, and $c\bar{c}\tau_\ell^+\tau_\ell^-$ looks similar to $b\bar{b}\tau_\ell^+\tau_\ell^-$. Right: The area-normalized $m_{\ell\ell}$ distribution for various X masses are shown. The distribution of $m_{\ell\ell}$ becomes less faithful to m_X as we increase the mass of X.

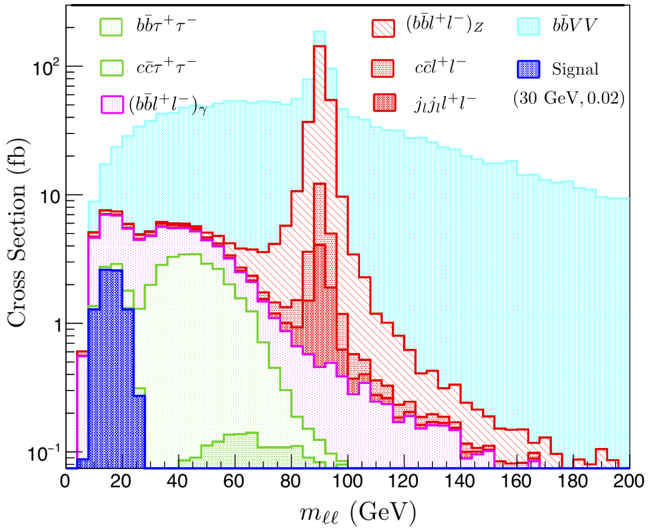

FIG. 5. The $m_{\ell\ell}$ distribution of the backgrounds scaled according to their cross section. The signal benchmark chosen for this plot is $(m_X, g_X) = (30\ \text{GeV}, 0.02)$. However, since the cross section of the signal is very small compared to the backgrounds, we multiplied the signal distribution by a factor of 10 to make it more visible in the plot. This distribution is only after the basic cuts. By imposing $m_{\ell\ell} < 25$, we can keep most of the signal, while throwing away a large portion of the background.

of this background is highly suppressed by the isolation cut $\Delta R(\ell^+, \ell^-) > 0.4$. The isolation cut also impacts the signal for small values of m_X; however, for all benchmarks we are considering ($m_X \geq 10$ GeV), imposing lepton isolation is more beneficial than relaxing it.

To understand the discriminatory power of the $m_{\ell\ell}$ cut, we plot the $m_{\ell\ell}$ of backgrounds normalized to the actual cross section in Fig. 5. The dark blue region is the distribution of the signal with $m_X = 30$ GeV. The cyan region belongs to the $b\bar{b}V_{\ell+\tau_\ell}V_{\ell+\tau_\ell}$ distribution, the red shaded region is the $b\bar{b}(\ell^+\ell^-)_Z$, and the magenta dotted distribution belongs to $b\bar{b}(\ell^+\ell^-)_\gamma$ distribution. The reducible backgrounds $c\bar{c}\ell^+\ell^-$ and $j_lj_l\ell^+\ell^-$ are also shown in red. The smooth green region belongs to $b\bar{b}\tau^+_\ell\tau^-_\ell$, and the dotted green distribution is for $c\bar{c}\tau^+_\ell\tau^-_\ell$. Only basic selections have been imposed on these distributions.

For our $m_X = 30$ GeV benchmark, imposing $m_{\ell\ell} < 25$ GeV eliminates 96% of the background while retaining 97% of the signal. For other m_X benchmarks, an appropriately optimized $m_{\ell\ell}$ cut performs similarly, though its effectiveness decreases for larger m_X. The decrease can be understood by looking at the $m_{\ell\ell}$ distribution for various m_X, shown in the right panel of Fig. 4. As we increase m_X, the $m_{\ell\ell}$ distribution broadens and gets more separated from the m_X value. The broadening occurs as a result of the allocation of the X's energy between leptons and neutrinos. The power of $m_{\ell\ell}$ in distinguishing the signal for each of the benchmarks is tabulated in Appendix A, where the upper bound on $m_{\ell\ell}$ (approximately $m_{\ell\ell} \lesssim 4/5 m_X$) has been optimized for each m_X value.

Another variable that is useful in signal-background discrimination is the azimuthal angle between the dilepton and the net missing energy vector $\Delta\phi(\ell\ell, \not{E}_T)$. Since leptons and neutrinos come from X, we expect to see some angular correlations between the leptons and the $\not{E}_T$ vector. Because we do not know the pseudorapidity of the transverse missing energy ($\not{E}_T$) vector, the distribution of the azimuthal angle provides a better discrimination than the total separation. A comparison between the two distributions of $\Delta R(\ell\ell, \not{E}_T)$ and $\Delta\phi(\ell\ell, \not{E}_T)$ is presented in Fig. 6. For the benchmarks with $m_X \leq 50$ GeV, the optimum cut seems to be $\Delta\phi(\ell\ell, \not{E}_T) \lesssim 0.5$.

Finally, we use the $\not{E}_T$ distribution to further discriminate between the signal and the background. As shown in Fig. 7, the signal favors the low $\not{E}_T$ regime. That is because $b\bar{b}X$

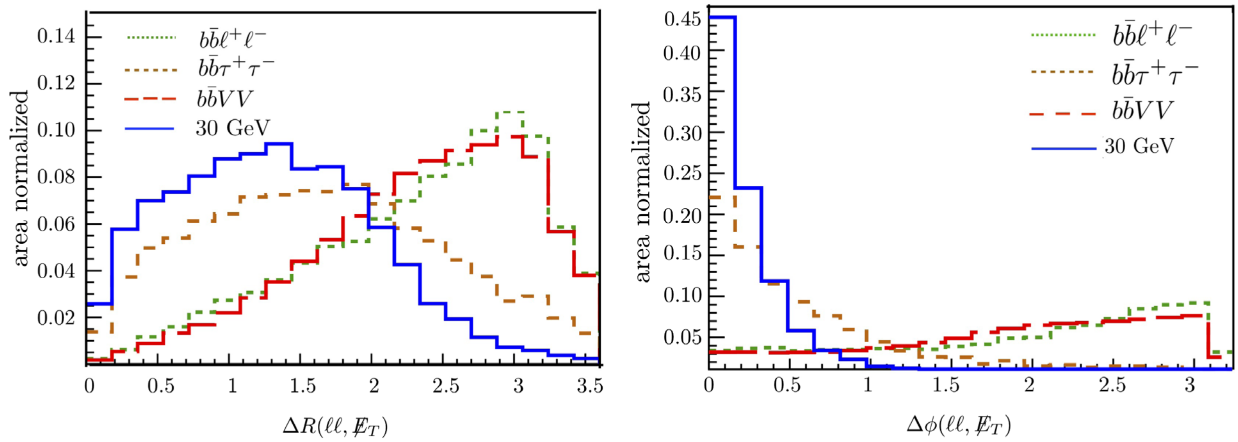

FIG. 6. The comparison between area-normalized $\Delta R(ll, \not{E}_T)$ (left) and $\Delta\phi(ll, \not{E}_T)$ (right) distributions. Only basic cuts have been imposed on these distributions. Even though these two plots are highly correlated, $\Delta\phi(ll, \not{E}_T)$ exhibits a better signal-background separation. That is because the pseudorapidity information of the $\not{E}_T$ vector is not available at the LHC. Due to the similar behavior of the reducible backgrounds with their corresponding irreducible background, their contribution is ignored in these plots.

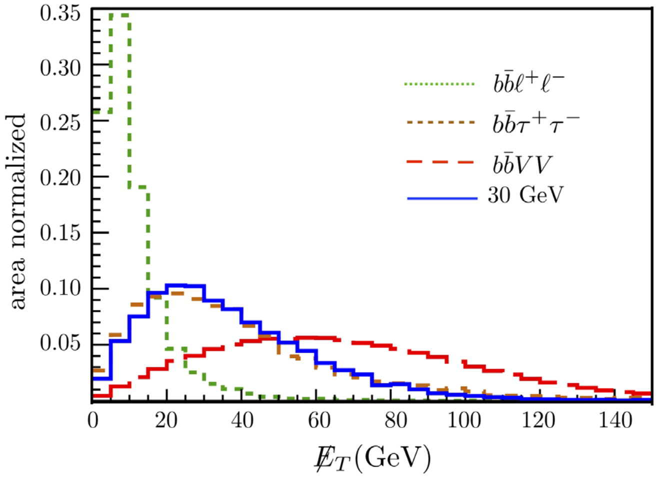

FIG. 7. The area-normalized distribution of the transverse missing energy after the basic cuts is shown. Similar to previous distribution plots, we have ignored the reducible background's contribution.

production is maximum near threshold, where X is almost stationary. The two neutrinos are, therefore, almost back to back, resulting in low $\not\!\!E_T$ in the signal. Thereby, we can impose an upper limit on $\not\!\!E_T$, to suppress $b\bar{b}V_{\ell+\tau_\ell}V_{\ell+\tau_\ell}$ and $b\bar{b}\tau_\ell^+\tau_\ell^-$ backgrounds.

Unfortunately, one background that favors low $\not\!\!E_T$ is $b\bar{b}\ell^+\ell^-$ because its $\not\!\!E_T$ is mostly a result of mismeasurement. To reduce this background, we must impose a lower bound on $\not\!\!E_T$ in addition to the upper bound. The exact upper and lower $\not\!\!E_T$ cuts were determined using our simulated events and adjusted to optimize the significance; the specific values for each of the benchmarks are presented in Appendix A; however, the cut on $\not\!\!E_T$ is roughly $10 \lesssim \not\!\!E_T \lesssim 70$ GeV.

To quantify the sensitivity of our search, we follow the conventional definitions:

$$\begin{aligned} S &\equiv \text{luminosity} \times \sigma(pp \to b\bar{b}\tau_\ell^+\tau_\ell^-)_{\text{X}} \times \kappa_{\text{signal}} \\ B &\equiv \text{luminosity} \times \{\sigma(pp \to b\bar{b}V_{\ell+\tau_\ell}V_{\ell+\tau_\ell})_{\text{SM}} \\ &\quad \times \kappa_{b\bar{b}V_{\ell+\tau_\ell}V_{\ell+\tau_\ell}} + \sigma(pp \to b\bar{b}\tau_\ell^+\tau_\ell^-)_{\text{SM}} \times \kappa_{b\bar{b}\tau^+\tau^-} \\ &\quad + \sigma(pp \to b\bar{b}\ell^+\ell^-) \times \kappa_{b\bar{b}\ell^+\ell^-}\}. \end{aligned} \tag{8}$$

In other words, S and B are, respectively, the number of signal and total background events (scaled to NLO rates) that we expect to observe at the LHC for a given luminosity and our cut flow. Using these, we quantify the discovery potential of our analysis using the significance, defined—following Ref. [83]—as

$$\text{Significance} = \frac{S}{\delta B} = \frac{S}{\sqrt{B + \sum_i \lambda_i^2 B^2}}, \tag{9}$$

where λ_i represent the systematic uncertainties associated with each background. We used the following values for λ_i, taken from the CMS leptonic $b\bar{b}V_{\ell+\tau_\ell}V_{\ell+\tau_\ell}$ search [84,85]: $\lambda_{b\bar{b}V_{\ell+\tau_\ell}V_{\ell+\tau_\ell}} = 5\%$, $\lambda_{b\bar{b}\tau^+\tau^-} = 10\%$, and $\lambda_{b\bar{b}\ell^+\ell^-} = 15\%$. Finally, it is important to note that we have ignored the effect of pileup in our analysis. Including the effect of pileup will likely affect the lower bound on $\not\!\!E_T$. Specifically, it will affect the contribution of the $b\bar{b}\ell^+\ell^-$ process in the background. However, the cross section of $b\bar{b}\ell^+\ell^-$ even before imposing the $\not\!\!E_T$ cut is already much smaller than other processes, and thus we do not expect that a small change in its cross section would alter our results significantly.

For each m_X benchmark, the cuts on the $m_{\ell\ell}$, $\Delta\phi(\ell\ell, \not\!\!E_T)$ and $\not\!\!E_T$ distributions have been optimized to yield the largest significance [Eq. (9)]. Once the cuts have been optimized, we use Eq. (5) to extrapolate the analysis to other g_X values and trace out contours of a desired significance, as shown in Fig. 8. The red lines are the bounds with (roughly) the current luminosity of the LHC—100 fb^{-1}—while the green lines are the projected sensitivity with the full luminosity of HL-LHC (3 ab^{-1}). The solid lines present the 3σ [letting the significance as defined in Eq. (9) be equal to 3] exclusion bound assuming the full systematical uncertainties mentioned earlier, and

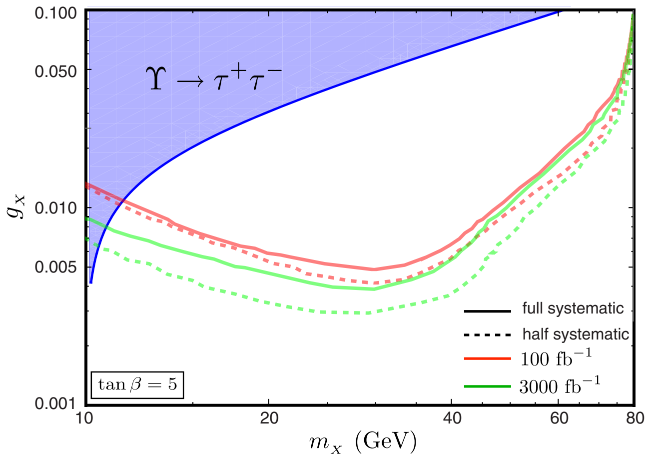

FIG. 8. By imposing an optimized cut on the mentioned variables, the LHC can probe the indicated parameter space up to 3σ significance, with 100 fb^{-1} integrated luminosity. The solid red line represents the significance with the systematic uncertainties mentioned in the section. The dashed red line is the significance when the systematic uncertainties are half. The green lines show the projected sensitivity at HL-LHC with 3 ab^{-1} integrated luminosity. The bound from $\Upsilon \to \tau^+\tau^-$ at *BABAR* [40] in shown in blue. Due to the low efficiency of the trigger cut, our sensitivity to very light m_X is weak; for 20 GeV $< m_X <$ 40 GeV, we have our maximum sensitivity, and then the sensitivity drops again as m_X increases due to a combination of a lower signal cross section and a decline in the discriminatory power of the cuts. In Sec. III A 1, we will motivate and study some variables that enhance the sensitivity to heavier m_X (>50 GeV). The presented bounds are for $\tan\beta = 5$. However, for any $\tan\beta > 1$, the sensitivity is almost the same.

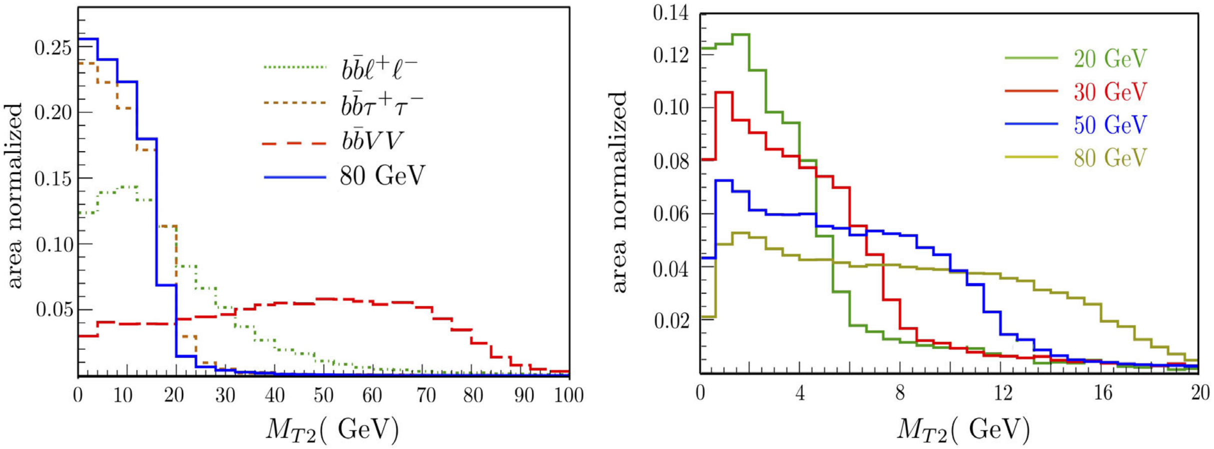

FIG. 9. The area-normalized distribution of various benchmarks (left) and the signal-backgrounds comparison (right) with respect to M_{T2} are shown. The signal prefers a small value of M_{T2}, whereas the $b\bar{b}V_{\ell+\tau_\ell}V_{\ell+\tau_\ell}$ backgrounds have a broad featureless distribution.

the dashed lines are 3σ significance when the systematic uncertainties are cut in half.

As we can see from Fig. 8, the LHC can probe a region of the parameter space that is out of reach of other current experiments. The LHC bounds are best in the mass range 20–40 GeV. The constraints on lighter X are milder, due to the low dilepton trigger efficiency and a relatively lower b-tagging efficiency, and the sensitivity for heavier X drops because the distribution of the signal and backgrounds becomes more similar, and so the cuts become less efficient.

Above 50 GeV, the limits worsen quickly. Therefore, it is worth exploring if there are any additional variables that can improve the bounds in the mass range 50 GeV $< m_X < m_Z$. The most troublesome background in this mass range is $b\bar{b}V_{\ell+\tau_\ell}V_{\ell+\tau_\ell}$, and the most important contribution to $b\bar{b}V_{\ell+\tau_\ell}V_{\ell+\tau_\ell}$ comes from $t\bar{t}$. The goal of the next subsection is to investigate some kinematic handles that specifically target the $t\bar{t}$ background.

1. Further separation of the signal from the $b\bar{b}V_{\ell+\tau_\ell}V_{\ell+\tau_\ell}$ background, for $m_X \sim m_Z$

The dominant background to our signal is $t\bar{t} \to b\bar{b}W^+_{\ell,\tau_\ell}W^-_{\ell,\tau_\ell}$. This background has some specific features that can help us separate this process from the signal. For example, the leptons and neutrinos in $t\bar{t}$ come from W decays, whereas in the signal they are due to τ decays. Therefore, M_{T2}, defined as

$$M_{T2} = \min_{\nu_T^1+\nu_T^2=\not{E}_T}(\max(M_T(\ell^+,\nu_1),M_T(\ell^-,\nu_2))), \quad (10)$$

with ν_T^i being the transverse momentum of the either sources of missing energy, should show a decent separation between the signal and the $t\bar{t}$ background. Since we are particularly interested in enhancing the sensitivity for $m_X \sim m_Z$, in the left panel of Fig. 9, we compare the distribution of the benchmark with $m_X = 80$ GeV with the backgrounds. As expected, M_{T2} of the signal prefers small values ($\lesssim$20 GeV), while M_{T2} for the $t\bar{t}$ background is approximately m_W. The distribution of M_{T2} for various benchmarks, after basic cuts only [so no $m_{\ell\ell}$, $\Delta\phi(\ell\ell,\not{E}_T)$, etc.], is also shown in the right panel of Fig. 9. Even though the separation of the signal from the $b\bar{b}V_{\ell+\tau_\ell}V_{\ell+\tau_\ell}$ background is more visible for lighter X, M_{T2} does not improve the bounds for $m_X < 50$ GeV compared to the combination of kinematic cuts introduced in the previous section. For heavy X, however, the efficiency of a cut on $\Delta\phi(\ell\ell,\not{E}_T)$ and $\not{E}_T$ distributions is not as efficient as a cut on M_{T2}. By requiring $M_{T2} < 16$ GeV, the significance goes up by a factor of 3 for $m_X = 80$ GeV, and the mild discrimination in the $\Delta\phi(\ell\ell,\not{E}_T)$ and $\not{E}_T$ distributions fade off. Therefore, we can no longer impose an efficient cut on $\Delta\phi(\ell\ell,\not{E}_T)$ and $\not{E}_T$ distributions.

Another attribute of the $t\bar{t}$ background is that there is an intimate relationship between b jets and leptons: $m_{bl} \lesssim m_t$. In the signal, on the other hand, such correlation does not exist, and m_{bl} can take any arbitrary values. To take advantage of this difference, we study $m_{b\ell}$ in Fig. 10, where the $b-\ell$ is one of the combinations that minimizes $(m_{\ell_i b_k} - m_t)^2 + (m_{\ell_j b_n} - m_t)^2)$, with $i \neq j$ and $k \neq n$. The distributions for $m_{b\ell}$ for the backgrounds and a $m_X = 80$ GeV benchmark are shown below in Fig. 10. We can see that there is a modest separation[12] between the $t\bar{t}$ background and other processes. A cut on this distribution can enhance the significance by 15% for the benchmark $(m_X, g_X) = (80\ \text{GeV}, 0.02)$.

To improve on this guess, we tried finding the neutrino momenta by reconstructing the W and top mass. In particular,

---

[12] According to the distributions in Fig. 10, the signal mostly resides in $m_{b\ell} \lesssim 200$ GeV, and thus the CMS search for third generation leptoquarks [63,64] with $m_{b\ell} > 250$ GeV does not have a noticeable sensitivity to our signal.

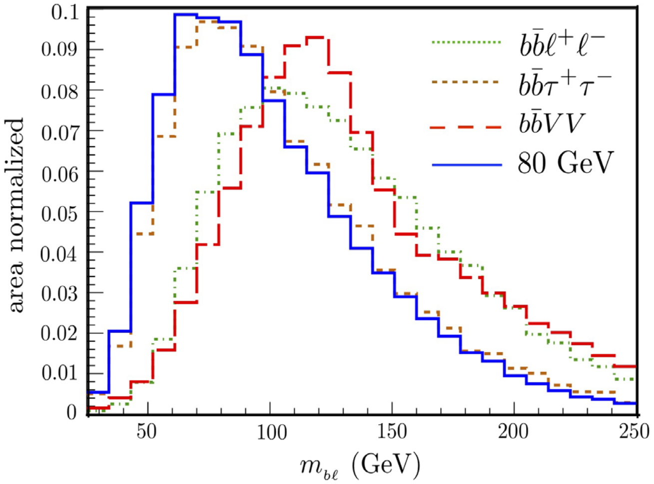

FIG. 10. The invariant mass of b and lepton that minimizes $(m_{\ell_i b_k} - m_t)^2 + (m_{\ell_j b_n} - m_t)^2$ is shown here. The distribution of both reconstructed tops is very similar, and so we are showing only one combination. The signal distribution, shown in solid blue, is for the benchmark $m_X = 80$ GeV. The most important background is $t\bar{t}$, shown in dashed red.

we scanned through all possible values of momenta that give the smallest χ^2, defined as

$$\chi^2 = \frac{(m^2_{\ell_i\nu_1} - m^2_W)^2}{\sigma^4_W} + \frac{(m^2_{\ell_j\nu_2} - m^2_W)^2}{\sigma^4_W} + \frac{(m^2_{b_k\ell_i\nu_1} - m^2_t)^2}{\sigma^4_t} + \frac{(m^2_{b_n\ell_j\nu_1} - m^2_t)^2}{\sigma^4_t}, \tag{11}$$

where σ_W and σ_t are arbitrary values we can use to enhance our discrimination. However, regardless of the values of $\sigma_{t,W}$, this method did not improve the signal-background discrimination. Therefore, the only cuts that could improve our sensitivity to $m_X \sim m_Z$ were $M_{T2} < 16$ GeV and $m_{bl} < 100$ GeV. With these cuts, more than 94% of the background is removed, while almost 50% of the signal is preserved. The effect of these cuts on the significance is shown in Fig. 11. Since the cross section is proportional to two factors of the coupling ($\sigma \propto g_X^2$), improving the limit by a factor of 4 translates into an improvement in the coupling by a factor of 2.

Having exhausted the cut-based search strategies for light m_X, we now turn to $m_X > m_Z$. In this regime, the τs coming from the decay of the X gauge boson are expected to be energetic enough that the resulting lepton from one of the τs can pass the single lepton trigger with high efficiency. Therefore, we study the semileptonic $b\bar{b}\tau_h\tau_\ell$.

B. Heavy X: $m_X > m_Z$

The cross section for X production falls as m_X increases. To compensate for the lower cross section, for $m_X > m_Z$, we shift final states to semileptonic τs (one tau decays to leptons, and one decays to hadrons) to take advantage of the higher branching ratio of τ to hadrons. The SM backgrounds we need to be concerned about are

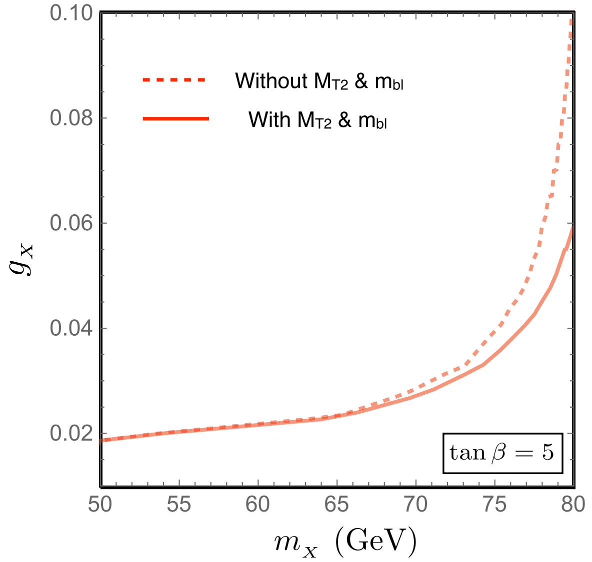

FIG. 11. The contribution of M_{T2} and m_{bl} to improving the sensitivity for $m_X = 80$ GeV. The dashed line indicates the 3σ significance with only the basic cuts and $25 < m_{\ell\ell} < 60$ GeV with 100 fb^{-1} integrated luminosity. The solid line is the 3σ significance with the same amount of luminosity with the basic cuts $+25 < m_{\ell\ell} < 60$ GeV $+ M_{T2} < 16$ GeV $+ m_{b\ell} < 100$ GeV. The extra cuts improve the sensitivity by roughly factor of 1.7.

$$\begin{aligned} &1)\ pp \to b\bar{b}W_{\tau_h}W^\pm_{\ell+\tau_\ell} \\ &2)\ pp \to b\bar{b}\tau_h\tau^\pm_\ell \\ &3)\ pp \to b\bar{b}W^\pm_{\ell+\tau_\ell} + \text{jets} \\ &4)\ pp \to b\bar{b}(Z/\gamma)_{\ell+\tau_\ell} + \text{jets}, \end{aligned} \tag{12}$$

where $\ell = e$, μ and τ_ℓ refers to the leptonic decay of a τ. Similarly, h represents the hadronic decay. Only the first two backgrounds mentioned in Eq. (12) are irreducible. As hadronic taus can be faked by "normal" jets $(=j_l + c + \bar{c} + b + \bar{b})$, we must include lepton + jet backgrounds such as 3 and 4 above.[13] To estimate the backgrounds with fake taus, we rely on the built-in tau identification algorithm in DELPHES, where we input matched samples.[14]

---

[13] Backgrounds 3 and 4 in Eq. (12) are separated as they contain different numbers of charged leptons. The third background has one lepton, and the fourth background contains two leptons, with some probability that one of the leptons falls outside of the acceptance and manifests itself as missing energy.

[14] We use MLM matching with MADGRAPH5+PYTHIA8, with XQCUT = 20 [86]. We have included up to two jets, e.g., $pp \to b\bar{b}W^\pm_{\ell+\tau_\ell} + 0, 1, 2$ jets. The matched/merged cross sections are then rescaled to the +0 jet NLO values.

As in the previous section, we must also consider backgrounds where a charm jet or a light-quark/gluon jet (j_l) is misidentified as a b jet. For example,

$$3.)\ pp \to b\bar{b}\,W^{\pm}_{\ell+\tau_\ell} + \text{jets} \Rightarrow \begin{cases} pp \to c\bar{c}W^{\pm}_{\ell+\tau_\ell} + \text{jets} \\ pp \to j_l j_l W^{\pm}_{\ell+\tau_\ell} + \text{jets} \end{cases}, \tag{13}$$

where “+jets” is treated as up to $+0-2$ jets.

To capture the interesting events, we impose the following conditions:

(i) Each event must include exactly one charged lepton that passes the single lepton trigger, $p_T(\ell_1) > 27(24)$ GeV, if the lepton is an electron (muon). We also require $|\eta(\ell)| < 2.5$.

(ii) We require one b jet possessing $p_T(j) > 50$ GeV, and $|\eta(j)| < 2.5$. As in the previous section, we use the DELPHES [78] b-identification algorithm to tag a b jet.

(iii) Every event must contain one tau-tagged hadronic jet, $p_T(j) > 50$ GeV, and $|\eta(j)| < 2.5$. As with b jets, we rely on the built-in algorithm in DELPHES [78]. We find the τ-tagging efficiency is roughly 40% for correctly identifying a hadronic τ with an approximately 0.3% risk of misidentifying a normal jet as a hadronic τ, for the processes being considered here.

(iv) In addition to the b jet and τ jet, the event may contain at most one additional jet, $p_T(j) > 50$ GeV, and $|\eta(j)| < 2.5$. The separation between each jet as well as the separation between all jets and the lepton must be greater than 0.4.

Due to the presence of multiple jets in our final state of interest, one might expect the main backgrounds come from tau-/b-misidentified jets. However, after requiring the basic cuts mentioned, the largest background is the irreducible $b\bar{b}W_{\tau_h}W^{\pm}_{\ell+\tau_\ell}$, 120 fb at NLO. The other sizable backgrounds are $b\bar{b}\tau_h\tau^{\pm}_{\ell}$, (3.5 fb), $b\bar{b}W^{\pm}_{\ell+\tau_\ell}$ + jets (3 fb), and $b\bar{b}(Z/\gamma)_{\ell+\tau_\ell}$ + jets (0.3 fb). All other backgrounds are negligible, $\ll 0.1$ fb.

To enhance the sensitivity of the signal further, we studied various kinematic distributions including M_{T2}, $m_{\ell j_i}$—where j_i is any of the jets in the final state, the separation between the lepton and the jets $\Delta R(\ell, j_i)$, the difference in the azimuthal angle between any two visible objects in the final state, as well as the p_T of each of the visible final states. Some of these distributions show a small difference between the signal and background, but none of them has a considerable effect on its own. Therefore, for this initial study, we will ignore the impact of these other distributions and quantify the sensitivity using the basic cuts alone. A multivariate analysis may be able to harness the slight differences across several kinematic distributions and yield increased sensitivity. Such an approach would be interesting to pursue, but is beyond the scope of the current work. However, as the differences in the distributions are very small, we expect the sensitivity gains achieved by a multi variant analysis (MVA) to be $\mathcal{O}(1)$ in the cross section and not orders of magnitude.

Using a similar definition of the signal and background as in Sec. III A,

$$\begin{aligned} S &\equiv \text{luminosity} \times \sigma(pp \to b\bar{b}\tau^+\tau^- \to b\bar{b}\ell^{\pm}j + 2\nu)_X \\ B &\equiv \text{luminosity} \times (\sigma(\bar{b}W_{\tau_h}W^{\pm}_{\ell+\tau_\ell})_{\text{SM}} \\ &\quad + \sigma(pp \to b\bar{b}\tau_h^{\pm}\tau_\ell^{\mp})_{\text{SM}} \\ &\quad + \sigma(pp \to b\bar{b}(W^{\pm}/Z/\gamma)_\ell + \text{jets}), \end{aligned}$$

with

$$\text{significance} = \frac{S}{\delta B} = \frac{S}{\sqrt{B + \lambda^2 B^2}},$$

and extrapolating to all values of g_X, $\tan\beta$ using Eq. (5), we can chart significance contours. In the $m_X > m_Z$ region, the main background is the irreducible background $pp \to t\bar{t} \to b\bar{b}W_{\tau h}W^{\pm}_{\ell+\tau_\ell}$, which has a systematic uncertainty of $\lambda = 12\%$ [56]. We will assume the same uncertainty on the rest of the backgrounds as well, though an $O(1)$ change in the systematic uncertainties of other backgrounds does not affect the results significantly. Assuming 100 fb^{-1} integrated luminosity, we can exclude up to $g_X \gtrsim 0.07$ for $m_X = 100$ GeV and $g_X \gtrsim 0.2$ for $m_X = 150$ GeV up to 3σ significance, illustrated in Fig. 12. This is about a factor of 2–4 improvement over previous constraints. Even though the total background of the semileptonic $b\bar{b}\tau_h\tau_\ell$ after the basic cuts is much smaller than that of the fully leptonic $b\bar{b}\tau_\ell\tau_\ell$, the constraints in the $m_X \ll m_Z$ region are much stronger. That is because in the $m_X \ll m_Z$ region the kinematic distributions of the signal have sharp features that distinguish it from the background. For larger masses, however, the distributions broaden and lose their sharp features, and thus separating the signal from the background is more challenging.

In general, a dedicated search at the LHC can improve the bounds by a factor of 2–10. These results can be achieved by studying simple kinematic distributions. With the use of a more advanced technique like a MVA, we might obtain even better results. Moreover, we have stopped our search at $m_X < 2m_W$. The bounds on a larger m_X will depend on some parameters in the scalar potential that we have ignored for our study (e.g., mixing between the scalars). If $m_X > 2m_t$, the decay of X to a pair of top quarks enjoys a significant probability as well as small background due to the large number of final state particles. These searches have already received some attention in several phenomenological studies [46–62]. The constraints obtained by these studies can be recast according to our choice of model parameter values.

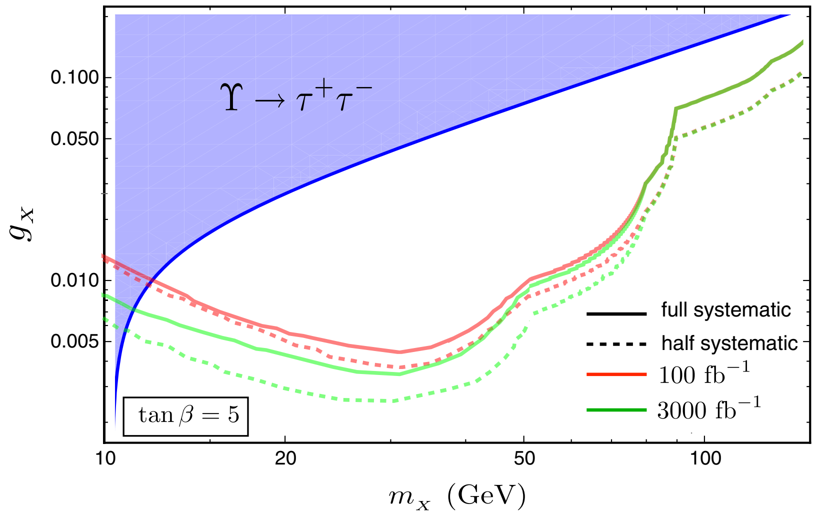

FIG. 12. The reach up to 3σ significance after 100 fb^{-1} integrated luminosity is shown. The current bound coming from $\Upsilon \to \tau^+\tau^-$ at *BABAR* [40] excludes the blue region.

IV. CONCLUSION

In this work, we explored the LHC potential to constrain X, the gauge boson associated with a spontaneously broken $U(1)^{(3)}_{B-L}$ symmetry. $U(1)^{(3)}_{B-L}$ symmetry is one of the simplest extensions of the SM, which was first proposed to explain the flavor alignment of the third generation of quarks. While X only interacts with the third generation of fermions in the interaction basis (at tree level), flavor nonuniversal couplings are generated once we rotate to the mass basis. These flavor-violating effects can be mitigated with certain charge assignments and coupling assumptions, but strong constrains from low-energy experiments persist for $m_X \leq 5$ GeV.

To hunt for heavier X, which are free from low-energy bounds, we developed two dedicated LHC search strategies based on $pp \to X, X \to \tau^+\tau^-$, a production and decay path that yields a high rate and numerous kinematic handles to suppress SM backgrounds. Following Ref. [32], we assume all scalars related to $U(1)^{(3)}_{B-L}$ breaking and the right-handed neutrino are heavy and focus on $m_X \leq 2m_W$ since this decouples the X phenomenology from any mixing in the scalar sector.

For $m_X < m_Z$, we find the optimal channel is where both taus decay leptonically. Using a combination of simple kinematic variables, such as $m_{\ell\ell}$, $\Delta\phi(ll, \not{E}_T)$ and $\not{E}_T$, we find that couplings as low as $g_X > 0.005$ for $m_X \sim 20$ GeV could be probed at 3σ sensitivity given 100 fb^{-1} integrated luminosity (roughly the current total LHC-13 luminosity). For heavier masses, the bounds are not as strong: $g_X > 0.05$ for $m_X \sim 80$ GeV probed at 3σ with the same amount of data. Extrapolating these bounds to the full HL-LHC luminosity of 3 ab^{-1}, we expect a further increase by a factor of 2 in the sensitivity (or $\sqrt{2}$ in g_X).

For $m_X > m_Z$, we find the semileptonic tau channel $(\tau_h^+\tau_\ell^- + \tau_\ell^+\tau_h^-)$ outperforms the fully leptonic mode; however, the number of pronounced kinematic differences between the signal and the dominant background ($pp \to t\bar{t}$) shrinks substantially. For 100 fb^{-1}, we find the 3σ exclusion limit reaches $g_X \gtrsim 0.1$ for $m_X = 100$ GeV and $g_X \gtrsim 0.2$ for $m_X = 150$ GeV. Both the low-mass and high-mass search strategies relied on cut-and-count methods, and it would be interesting to explore what improvements multivariate techniques can squeeze out.

ACKNOWLEDGMENTS

We are particularly thankful to S. Chenarani for the numerous insightful conversations. We would like to also thank H. Hesari, S. Khatibi, J. H. Kim, M. Paktinat, and F. Rezai for their useful comments. We are grateful to CERN theory group for their hospitality. The work of A. M. was partially supported by the National Science Foundation under Grants No. PHY-1820860.

APPENDIX A: THE CUT FLOW OF BENCHMARKS WITH $m_X < m_X$

The cut flow on each of the benchmarks is shown in Table III ($m_X = 10$ GeV), Table IV ($m_X = 20$ GeV), Table V ($m_X = 30$ GeV), Table VI ($m_X = 50$ GeV), and Table VII ($m_X = 80$ GeV). The quoted cross sections are at NLO, even though the events are LO. We generated 10^6 events for the signal, $b\bar{b}\ell^+\ell^-$, and $b\bar{b}\tau_\ell^+\tau_\ell^-$ processes. Due to the higher cross section of $b\bar{b}V_{\ell+\tau_\ell}V_{\ell+\tau_\ell}$, we generated 2×10^6 events for this process. In all of the benchmarks studied here, $m_{\ell\ell}$ proved to be a useful variable in distinguishing the signal. For $m_X \leq 50$ GeV, we used $\Delta\phi(\ell\ell, \not{E}_T)$ and $\not{E}_T$ to further distinguish the signal, and for $m_X = 80$ GeV, we found M_{T2} to be a more useful variable. Each cut has been optimized such that it gives the highest significance, defined in Eq. (9).

TABLE III. The cut flow for $m_X = 10$ GeV. The cross section of this benchmark is small after the basic selection. However, the $m_{\ell\ell}$ cut efficiently enhances the signal-to-background ratio.

	X_μ	SM backgrounds (fb)			
Cuts	(10 GeV, 0.02)	$b\bar{b}\ell^+\ell^-$	$b\bar{b}V_{\ell+\tau_\ell}V_{\ell+\tau_\ell}$	$b\bar{b}\tau^+\tau^-$	Significance$\|_{\mathcal{L}=100\ \mathrm{fb}^{-1}}$
Basic selection	0.61	282.6	1365.8	32.2	0.005
$m_{\ell\ell} < 10$ GeV	0.5	0.5	1.55	0.03	2.3
$\Delta\phi(\ell\ell, \not{E}_T) < 0.5$	0.3	0.05	0.26	0.03	4.6
5 GeV $< \not{E}_T <$ 70 GeV	0.3	0.03	0.21	0.03	5.3
Efficiencies	50%	0.01%	0.016%	0.1%	

TABLE IV. The effect of each cut on the signal with $m_X = 20$ GeV and the backgrounds. The $m_{\ell\ell}$ cut efficiently enhances the signal-to-background ratio.

	X_μ	SM backgrounds (fb)			
Cuts	(20 GeV, 0.02)	$b\bar{b}\ell^+\ell^-$	$b\bar{b}V_{\ell+\tau_\ell}V_{\ell+\tau_\ell}$	$b\bar{b}\tau^+\tau^-$	Significance$\|_{\mathcal{L}=100\ \mathrm{fb}^{-1}}$
Basic selection	2.27	282.6	1365.8	32.2	0.02
$m_{\ell\ell} < 15$ GeV	2.04	1.88	12.33	0.16	2.00
$\Delta\phi(\ell\ell, \not{E}_T) < 0.5$	1.69	0.23	0.44	0.13	12.9
$10 < \not{E}_T < 70$	1.67	0.06	0.30	0.07	21.0
Efficiencies	73.2%	0.02%	0.02%	0.27%	

TABLE V. The effect of each cut on the signal with $m_X = 30$ GeV and the backgrounds. The $m_{\ell\ell}$ cut efficiently enhances the signal-to-background ratio.

	X_μ	SM backgrounds (fb)			
Cuts	(30 GeV, 0.02)	$b\bar{b}\ell^+\ell^-$	$b\bar{b}V_{\ell+\tau_\ell}V_{\ell+\tau_\ell}$	$b\bar{b}\tau^+\tau^-$	Significance$\|_{\mathcal{L}=100\ \mathrm{fb}^{-1}}$
Basic selection	8.13	282.6	1365.8	32.2	0.07
$m_{\ell\ell} < 25$ GeV	7.9	3.95	12.82	0.24	5.77
$\Delta\phi(\ell\ell, \not{E}_T) < 0.53$	6.4	0.32	0.44	0.19	40.0
$13 < \not{E}_T < 60$	5.48	0.21	0.31	0.11	49.0
Efficiencies	67.4%	0.04%	0.01%	0.3%	

TABLE VI. The effect of each cut on the signal with $m_X = 50$ GeV and the backgrounds.

	X_μ	SM backgrounds (fb)			
Cuts	(50 GeV, 0.02)	$b\bar{b}\ell^+\ell^-$	$b\bar{b}V_{\ell+\tau_\ell}V_{\ell+\tau_\ell}$	$b\bar{b}\tau^+\tau^-$	Significance$\|_{\mathcal{L}=100\ \mathrm{fb}^{-1}}$
Basic selection	3.42	282.6	1365.8	32.2	0.03
$10 < m_{\ell\ell} < 35$ GeV	2.88	6.35	163	5.58	0.27
$\Delta\phi(\ell\ell, \not{E}_T) < 0.5$	2.08	0.74	7.07	3.38	1.37
$22 < \not{E}_T < 75$	1.75	0.03	6.5	0.3	3.5
Efficiencies	51%	0.01%	0.48%	1.17%	

TABLE VII. The effect of each cut on the signal with $m_X = 80$ GeV and the backgrounds. To further enhance the signal-to-background ratio, M_{T2} and $m_{b\ell}$ is used.

	X_μ	SM backgrounds (fb)			
Cuts	(80 GeV, 0.02)	$b\bar{b}\ell^+\ell^-$	$b\bar{b}V_{\ell+\tau_\ell}V_{\ell+\tau_\ell}$	$b\bar{b}\tau^+\tau^-$	Significance$\vert_{\mathcal{L}=100\ \mathrm{fb}^{-1}}$
Basic selection	2.8	282.6	1365.8	32.2	0.02
$25 < m_{\ell\ell} < 60$ GeV	2.51	2.58	317.2	21.25	0.11
$M_{T2} < 16$ GeV	2.24	1.6	41.3	17.3	0.30
$m_{b\ell} < 100$ GeV	1.15	0.56	10.3	8.8	0.35
Efficiencies	41.1%	0.2%	0.8%	27.3%	

APPENDIX B: LAGRANGIAN

The new terms to the Lagrangians are the following:

$$\begin{aligned}
\mathcal{L}_{\rm new} &= |D_\mu^\phi \phi|^2 + |D_\mu^s s|^2 + \mathcal{L}_{\rm yuk} - V(H,\phi,s)\\
\mathcal{L}_{\rm yuk} &= \bar{\mathbf{Q}}_L \begin{pmatrix} y_{11}^u\tilde{H} & y_{12}^u\tilde{H} & y_{13}^u\tilde{\phi}\\ y_{21}^u\tilde{H} & y_{22}^u\tilde{H} & y_{23}^u\tilde{\phi}\\ 0 & 0 & y_{33}^u\tilde{H}\end{pmatrix}\mathbf{u}_R\\
&\quad + \bar{\mathbf{Q}}_L \begin{pmatrix} y_{11}^d H & y_{12}^d H & 0\\ y_{21}^d H & y_{22}^d H & 0\\ y_{31}^d\phi & y_{32}^d\phi & y_{33}^d H\end{pmatrix}\mathbf{d}_R + \text{H.c.}\\
&\quad + \frac{1}{\Lambda^2}(\bar{L}_3\tilde{\phi})(\phi^\dagger \tilde{L}_{1,2})s^\star\\
V(H,\phi,s) &= V(H) - \mu_\phi^2|\phi_2|^2 + \frac{\lambda_\phi}{2}|\phi|^4 + \lambda_{\phi h}|H|^2|\phi|^2\\
&\quad + \lambda'_{\phi h}(\phi^\dagger H)(H^\dagger\phi) - \mu_s^2|s|^2 + \frac{\lambda_s}{2}|s|^4\\
&\quad + \lambda_{hs}|H|^2|s|^2 + \lambda_{\phi s}|\phi|^2|s|^2\\
&\quad - [\mu(\phi^\dagger H)s + \text{H.c.}],
\end{aligned}$$

where

$$\begin{aligned}
D_\mu^\phi\phi &= \left(\partial_\mu - ig\frac{\tau_i}{2}W_\mu^i - i\frac{g'}{2}B_\mu - i\frac{g_X}{3}X_\mu\right)\phi\\
D_\mu^s s &= \left(\partial_\mu - i\frac{g_X}{3}X_\mu\right)s,
\end{aligned}$$

where g_X is the gauge coupling associated with $U(1)_{B-L}^{(3)}$. Due to the charge of the third generation of fermions, some of the Yukawa interactions involve Higgs, and the mixings of third generation of fermions involve ϕ. Since the charge of leptons under $U(1)_{B-L}^{(3)}$ is -1, we need multiple ϕ and s to cancel its charge under $U(1)_{B-L}^{(3)}$. Therefore, the mixings of leptons only occur at the nonrenormalizable level. It is worth mentioning that there is no mixing between charged leptons.

APPENDIX C: REPRODUCING THE CKM MATRIX AND FLAVOR-CHANGING INTERACTIONS OF *X*

This model was first suggested in Ref. [32], and the details of the model are somewhat complicated and lengthy. Rather than discussing all of the moving parts, we will focus on the generation of the CKM matrix and potential FCNCs.

Because the third generation is charged under $U(1)_{B-L}^{(3)}$ while the first and second generations are not, mixing among generations requires ϕ. The full Yukawa interaction, including interactions with Higgs or ϕ and working in a basis with diagonal kinetic terms, can be written as

$$\begin{aligned}
Ł_{\rm yuk}^q &= \bar{\mathbf{Q}}_L \begin{pmatrix} y_{11}^u\tilde{H} & y_{12}^u\tilde{H} & y_{13}^u\tilde{\phi}\\ y_{21}^u\tilde{H} & y_{22}^u\tilde{H} & y_{23}^u\tilde{\phi}\\ 0 & 0 & y_{33}^u\tilde{H}\end{pmatrix}\mathbf{u}_R\\
&\quad + \bar{\mathbf{Q}}_L \begin{pmatrix} y_{11}^d H & y_{12}^d H & 0\\ y_{21}^d H & y_{22}^d H & 0\\ y_{31}^d\phi & y_{32}^d\phi & y_{33}^d H\end{pmatrix}\mathbf{d}_R + \text{H.c.} \qquad \text{(C1)}
\end{aligned}$$

The upper 2×2 block of both quark mass matrices can be brought to diagonal form by rotations among $Q_{1,2}$, $u_{R,1,2}$ and $d_{R,1,2}$. Note that, after these rotations—call them $R_{12}^{uL,dL}$—the up-type quark mass matrix has nonzero (1, 3), (2, 3) entries, while the down-type matrix has the opposite structure:

$$\begin{aligned}
R_{12}^{uL}.M_u.R_{12}^{uR\dagger} &= \begin{pmatrix} m_u^0 & 0 & cm_t^0\\ 0 & m_c^0 & dm_t^0\\ 0 & 0 & m_t^0\end{pmatrix} \quad \text{and}\\
R_{12}^{dL}.M_d.R_{12}^{dR\dagger} &= \begin{pmatrix} m_d^0 & 0 & 0\\ 0 & m_s^0 & 0\\ am_b^0 & bm_b^0 & m_b^0.\end{pmatrix}, \qquad \text{(C2)}
\end{aligned}$$

This structure follows automatically from the $U(1)_{B-L}^{(3)}$ charge of ϕ. Given this structure, bringing the mass matrices to fully diagonal form can be accomplished by redefinitions among left-handed fermions between Q_3 and $Q_{1,2}$ and redefinitions among the right -handed down quarks between d_{R3} and $d_{R,1,2}$. As the kinetic terms of the three generations are not identical, these last redefinitions generically induce FCNCs in $U(1)^{(3)}_{B-L}$ gauge interactions. These FCNCs are tightly constrained, especially in the down-quark sector. However, if we impose that $a, b \simeq 0$ in Eq. (C2), all FCNCs are relegated to the up-quark sector, where constraints are weaker. In this circumstance, a viable (3×3) CKM matrix is still generated, and one can show that the elements of the up-quark matrix in Eq. (C2) are proportional to the CKM elements $c \sim V_{ub}$ and $d \sim V_{cb}$ [32].

We emphasize that the choice $a \sim b \sim 0$ is not demanded by the setup but is a phenomenological constraint. Accepting this constraint, we can work out the fermion mass basis interactions with X. The only place where FCNC $U(1)^{(3)}_{B-L}$ interactions occur is with left-handed up quarks. Specifically, expanding out the kinetic term and performing the rotations described above to go to the mass basis,

$$\mathcal{L}^{\text{tree}}_{XQQ} \simeq \frac{g_X}{3}\bar{u}_L \begin{pmatrix} V_{ub}^2 & V_{ub}V_{cb} & V_{ub} \\ V_{ub}V_{cb} & V_{cb}^2 & V_{cb} \\ V_{ub} & V_{cb} & 1 \end{pmatrix} \gamma^\mu u_L X_\mu + \frac{g_X}{3}\bar{d}_L \begin{pmatrix} 0 & 0 & 0 \\ 0 & 0 & 0 \\ 0 & 0 & 1 \end{pmatrix} \gamma^\mu d_L X_\mu. \tag{C3}$$

There are no off-diagonal terms present in the u_R, d_R, or leptonic interactions with X, so they all have the same form as the d_L interaction in Eq. (C3).

---

[1] R. Foot, New physics from electric charge quantization?, Mod. Phys. Lett. A **06**, 527 (1991).

[2] X. G. He, G. C. Joshi, H. Lew, and R. R. Volkas, New Z' phenomenology, Phys. Rev. D **43**, R22 (1991).

[3] X.-G. He, G. C. Joshi, H. Lew, and R. R. Volkas, Simplest Z' model, Phys. Rev. D **44**, 2118 (1991).

[4] R. Foot, X. G. He, H. Lew, and R. R. Volkas, Model for a light Z' boson, Phys. Rev. D **50**, 4571 (1994).

[5] R. Alonso, P. Cox, C. Han, and T. T. Yanagida, Anomaly-free local horizontal symmetry and anomaly-full rare B-decays, Phys. Rev. D **96**, 071701 (2017).

[6] J. C. Pati and A. Salam, Lepton number as the fourth color, Phys. Rev. D **10**, 275 (1974); Erratum, Phys. Rev. D **11**, 703 (E) (1975).

[7] R. E. Marshak and R. N. Mohapatra, Quark–Lepton symmetry and $B-L$ as the U(1) generator of the electroweak symmetry group, Phys. Lett. **91B**, 222 (1980).

[8] F. Wilczek and A. Zee, Conservation or violation of $B-L$ in proton decay, Phys. Lett. **88B**, 311 (1979).

[9] R. N. Mohapatra and R. E. Marshak, Local $B-L$ Symmetry of Electroweak Interactions, Majorana Neutrinos and Neutron Oscillations, Phys. Rev. Lett. **44**, 1316 (1980); Erratum, Phys. Rev. Lett.**44**, 1643(E) (1980).

[10] A. E. Nelson and J. Walsh, Short baseline neutrino oscillations and a new light gauge boson, Phys. Rev. D **77**, 033001 (2008).

[11] R. Harnik, J. Kopp, and P. A. N. Machado, Exploring ν signals in dark matter detectors, J. Cosmol. Astropart. Phys. 07 (2012) 026.

[12] P. del Amo Sanchez *et al.* (*BABAR* Collaboration), Test of Lepton Universality in $\Upsilon(1S)$ Decays at BABAR, Phys. Rev. Lett. **104**, 191801 (2010).

[13] K. S. Babu and Y. Meng, Flavor violation in supersymmetric Q(6) model, Phys. Rev. D **80**, 075003 (2009).

[14] K. S. Babu and S. Nandi, Natural fermion mass hierarchy and new signals for the Higgs boson, Phys. Rev. D **62**, 033002 (2000).

[15] E. Golowich, J. Hewett, S. Pakvasa, and A. A. Petrov, Relating $\mathrm{D}^0-\bar{\mathrm{D}}^0$ mixing and $\mathrm{D}^0 \to \mathrm{l}^+\mathrm{l}^-$ with new physics, Phys. Rev. D **79**, 114030 (2009).

[16] S. Baek, N. G. Deshpande, X. G. He, and P. Ko, Muon anomalous $g-2$ and gauged $L_\mu - L_\tau$ models, Phys. Rev. D **64**, 055006 (2001).

[17] E. Ma, D. P. Roy, and S. Roy, Gauged $L_\mu - L_\tau$ with large muon anomalous magnetic moment and the bimaximal mixing of neutrinos, Phys. Lett. B **525**, 101 (2002).

[18] E. Salvioni, A. Strumia, G. Villadoro, and F. Zwirner, Non-universal minimal Z' models: present bounds and early LHC reach, J. High Energy Phys. 03 (2010) 010.

[19] J. Heeck and W. Rodejohann, Gauged $L_\mu - L_\tau$ symmetry at the electroweak scale, Phys. Rev. D **84**, 075007 (2011).

[20] K. Harigaya, T. Igari, M. M. Nojiri, M. Takeuchi, and K. Tobe, Muon $g-2$ and LHC phenomenology in the $L_\mu - L_\tau$ gauge symmetric model, J. High Energy Phys. 03 (2014) 105.

[21] C. D. Carone, Flavor-nonuniversal dark gauge bosons and the muon $g-2$, Phys. Lett. B **721**, 118 (2013).

[22] A. Crivellin, G. D'Ambrosio, and J. Heeck, Addressing the LHC flavor anomalies with horizontal gauge symmetries, Phys. Rev. D **91**, 075006 (2015).

[23] W. Altmannshofer, M. Carena, and A. Crivellin, $L_\mu - L_\tau$ theory of Higgs flavor violation and $(g-2)_\mu$, Phys. Rev. D **94**, 095026 (2016).

[24] W. Altmannshofer, S. Gori, M. Pospelov, and I. Yavin, Quark flavor transitions in $L_\mu - L_\tau$ models, Phys. Rev. D **89**, 095033 (2014).

[25] Y. Farzan, A model for large non-standard interactions of neutrinos leading to the LMA-dark solution, Phys. Lett. B **748**, 311 (2015).

[26] A. Crivellin, G. D'Ambrosio, and J. Heeck, Explaining $h \to \mu^\pm\tau^\mp$, $B \to K^*\mu^+\mu^-$ and $B \to K\mu^+\mu^-/B \to Ke^+e^-$ in a Two-Higgs-Doublet Model with Gauged $L_\mu - L_\tau$, Phys. Rev. Lett. **114**, 151801 (2015).

[27] Y. Farzan and I. M. Shoemaker, Lepton flavor violating non-standard interactions via light mediators, J. High Energy Phys. 07 (2016) 033.

[28] F. Elahi and A. Martin, Using the modified matrix element method to constrain $L_\mu - L_\tau$ interactions, Phys. Rev. D **96**, 015021 (2017).

[29] F. Elahi and A. Martin, Constraints on $L_\mu - L_\tau$ interactions at the LHC and beyond, Phys. Rev. D **93**, 015022 (2016).

[30] E. J. Chun, A. Das, J. Kim, and J. Kim, Searching for flavored gauge bosons, J. High Energy Phys. 02 (2019) 093.

[31] R. Alonso, P. Cox, C. Han, and T. T. Yanagida, Flavoured $B-L$ local symmetry and anomalous rare B decays, Phys. Lett. B **774**, 643 (2017).

[32] K. S. Babu, A. Friedland, P. A. N. Machado, and I. Mocioiu, Flavor gauge models below the fermi scale, J. High Energy Phys. 12 (2017) 096.

[33] P. Cox, C. Han, and T. T. Yanagida, LHC search for right-handed neutrinos in Z' models, J. High Energy Phys. 01 (2018) 037.

[34] P. Cox, C. Han, and T. T. Yanagida, Right-handed neutrino dark matter in a U(1) extension of the Standard Model, J. Cosmol. Astropart. Phys. 01 (2018) 029.

[35] A. Dev and R. N. Mohapatra, Natural alignment of quark flavors and radiatively induced quark mixings, Phys. Rev. D **98**, 073002 (2018).

[36] V. V. Anisimovsky *et al.*, Improved Measurement of the $K^+ \to \pi^+ v\bar{v}$ Anti-nu Branching Ratio, Phys. Rev. Lett. **93**, 031801 (2004).

[37] A. V. Artamonov *et al.* (E949 Collaboration), New Measurement of the $K^+ \to \pi^+\nu\bar{\nu}$ Branching Ratio, Phys. Rev. Lett. **101**, 191802 (2008).

[38] M. Ablikim *et al.* (BESIII Collaboration), Precision measurement of the mass of the τ lepton, Phys. Rev. D **90**, 012001 (2014).

[39] P. Vilain *et al.* (CHARM-II Collaboration), Precision measurement of electroweak parameters from the scattering of muon-neutrinos on electrons, Phys. Lett. B **335**, 246 (1994).

[40] P. del Amo Sanchez *et al.* (*BABAR* Collaboration), Test of Lepton Universality in $\Upsilon(1S)$ Decays at BABAR, Phys. Rev. Lett. **104**, 191801 (2010).

[41] M. Aaboud *et al.* (ATLAS Collaboration), Search for WW/WZ resonance production in $\ell\nu qq$ final states in pp collisions at $\sqrt{s} = 13$ TeV with the ATLAS detector, J. High Energy Phys. 03 (2018) 042.

[42] A. M. Sirunyan *et al.* (CMS Collaboration), Search for massive resonances decaying into WW, WZ, ZZ, qW, and qZ with dijet final states at $\sqrt{s} = 13$ TeV, Phys. Rev. D **97**, 072006 (2018).

[43] A. M. Sirunyan *et al.* (CMS Collaboration), Combination of searches for heavy resonances decaying to WW, WZ, ZZ, WH, and ZH boson pairs in proton?proton collisions at $\sqrt{s} = 8$ and 13 TeV, Phys. Lett. B **774**, 533 (2017).

[44] CMS Collaboration, Search for massive resonances decaying into WW, WZ,ZZ, qW, and qZ in the dijet final state at $\sqrt{s} = 13$ TeV, Phys. Rev. D **97**, 072006 (2018).

[45] N. V. Biesuz (ATLAS Collaboration), Exotic diboson searches in the $\ell\nu\nu qq$ final state using data at $\sqrt{s} =$ 13 TeV collected with the ATLAS detector, Proc. Sci., EPS-HEP2017 (**2017**) 683.

[46] C. T. Hill, Topcolor: Top quark condensation in a gauge extension of the standard model, Phys. Lett. B **266**, 419 (1991).

[47] C. T. Hill and S. J. Parke, Top production: Sensitivity to new physics, Phys. Rev. D **49**, 4454 (1994).

[48] C. T. Hill, Topcolor assisted technicolor, Phys. Lett. B **345**, 483 (1995).

[49] R. M. Harris and S. Jain, Cross sections for leptophobic topcolor Z' decaying to top-Antitop, Eur. Phys. J. C **72**, 2072 (2012).

[50] J. L. Rosner, Prominent decay modes of a leptophobic Z', Phys. Lett. B **387**, 113 (1996).

[51] K. R. Lynch, E. H. Simmons, M. Narain, and S. Mrenna, Finding Z' bosons coupled preferentially to the third family at LEP and the Tevatron, Phys. Rev. D **63**, 035006 (2001).

[52] M. Carena, A. Daleo, B. A. Dobrescu, and T. M. P. Tait, Z' gauge bosons at the Tevatron, Phys. Rev. D **70**, 093009 (2004).

[53] D. Choudhury, R. M. Godbole, R. K. Singh, and K. Wagh, Top production at the Tevatron/LHC and nonstandard, strongly interacting spin one particles, Phys. Lett. B **657**, 69 (2007).

[54] V. Khachatryan *et al.* (CMS Collaboration), Search for resonant $t\bar{t}$ production in proton-proton collisions at $\sqrt{s} =$ 8 TeV, Phys. Rev. D **93**, 012001 (2016).

[55] CMS Collaboration, Search for $t\bar{t}$ resonances at the HL-LHC and HE-LHC with the Phase-2 CMS detector, Report No. CMS-PAS-FTR-18-009.

[56] M. Aaboud *et al.* (ATLAS Collaboration), Search for heavy particles decaying into top-quark pairs using lepton-plus-jets events in proton-proton collisions at $\sqrt{s} = 13$ TeV with the ATLAS detector, Eur. Phys. J. C **78**, 565 (2018).

[57] A. M. Sirunyan *et al.* (CMS Collaboration), Search for $\mathrm{t\bar{t}}$ resonances in highly boosted lepton + jets and fully hadronic final states in proton-proton collisions at $\sqrt{s} = 13$ TeV, J. High Energy Phys. 07 (2017) 001.

[58] A. M. Sirunyan *et al.* (CMS Collaboration), Measurement of the jet mass in highly boosted $\mathrm{t\bar{t}}$ events from pp collisions at $\sqrt{s} = 8$ TeV, Eur. Phys. J. C **77**, 467 (2017).

[59] L. Cerrito, D. Millar, S. Moretti, and F. Span, Discovering and profiling Z' bosons using asymmetry observables in top quark pair production with the lepton-plus-jets final state at the LHC, arXiv:1609.05540.

[60] C. Arina *et al.*, A comprehensive approach to dark matter studies: Exploration of simplified top-philic models, J. High Energy Phys. 11 (2016) 111.

[61] K. Pedersen and Z. Sullivan, μ_x boosted-bottom-jet tagging and Z' boson searches, Phys. Rev. D **93**, 014014 (2016).

[62] P. J. Fox, I. Low, and Y. Zhang, Top-philic Z' forces at the LHC, J. High Energy Phys. 03 (2018) 074.

[63] CMS Collaboration, Prospects for exclusion or discovery of a third generation leptoquark decaying into a τ lepton and a b quark with the upgraded CMS detector at the HL-LHC, Report No. CMS-PAS-FTR-18-028.

[64] V. Khachatryan *et al.* (CMS Collaboration), Search for pair production of third-generation scalar leptoquarks and top

squarks in proton-proton collisions at $\sqrt{s} = 8$ TeV, Phys. Lett. B **739**, 229 (2014).
[65] A. M. Sirunyan *et al.* (CMS Collaboration), Search for Higgs boson pair production in the $bb\tau\tau$ final state in proton-proton collisions at $\sqrt{(s)} = 8$ TeV, Phys. Rev. D **96**, 072004 (2017).
[66] A. M. Sirunyan *et al.* (CMS Collaboration), Combination of Searches for Higgs Boson Pair Production in Proton-Proton Collisions at $\sqrt{s} = 13$ TeV, Phys. Rev. Lett. **122**, 121803 (2019).
[67] L. Cadamuro, Search for Higgs boson pair production in the $b\bar{b}\tau^+\tau^-$ decay channel with the CMS detector at the LHC, Ph.D. thesis, University Paris-Saclay, 2017.
[68] M. R. Whalley, A compilation of data on hadronic total cross sections in ee interactions, J. Phys. G **29**, A1 (2003).
[69] V. Khachatryan *et al.* (CMS Collaboration), Search for new physics in final states with two opposite-sign, same-flavor leptons, jets, and missing transverse momentum in pp collisions at $\sqrt{s} = 13$ TeV, J. High Energy Phys. 12 (2016) 013.
[70] V. Khachatryan *et al.* (CMS Collaboration), Measurement of the $t\bar{t}$ production cross section using events in the eμ final state in pp collisions at $\sqrt{s} = 13$ TeV, Eur. Phys. J. C **77**, 172 (2017).
[71] M. Aaboud *et al.* (ATLAS Collaboration), Search for the Dimuon Decay of the Higgs Boson in pp Collisions at $\sqrt{s} = 13$ TeV with the ATLAS Detector, Phys. Rev. Lett. **119**, 051802 (2017).
[72] M. Aaboud *et al.* (ATLAS Collaboration), Search for new high-mass phenomena in the dilepton final state using 36 fb^1 of proton-proton collision data at $\sqrt{s} = 13$ TeV with the ATLAS detector, J. High Energy Phys. 10 (2017) 182.
[73] C. Degrande, C. Duhr, B. Fuks, D. Grellscheid, O. Mattelaer, and T. Reiter, UFO—The Universal FeynRules output, Comput. Phys. Commun. **183**, 1201 (2012).
[74] A. Alloul, N. D. Christensen, C. Degrande, C. Duhr, and B. Fuks, FeynRules 2.0–A complete toolbox for tree-level phenomenology, Comput. Phys. Commun. **185**, 2250 (2014).
[75] J. Alwall, R. Frederix, S. Frixione, V. Hirschi, F. Maltoni, O. Mattelaer, H. S. Shao, T. Stelzer, P. Torrielli, and M. Zaro, The automated computation of tree-level and next-to-leading order differential cross sections, and their matching to parton shower simulations, J. High Energy Phys. 07 (2014) 079.
[76] J. Alwall, M. Herquet, F. Maltoni, O. Mattelaer, and T. Stelzer, MadGraph 5: Going Beyond, J. High Energy Phys. 06 (2011) 128.
[77] T. Sjstrand, S. Ask, J. R. Christiansen, R. Corke, N. Desai, P. Ilten, S. Mrenna, S. Prestel, C. O. Rasmussen, and P. Z. Skands, An introduction to PYTHIA 8.2, Comput. Phys. Commun. **191**, 159 (2015).
[78] J. de Favereau, C. Delaere, P. Demin, A. Giammanco, V. Lematre, A. Mertens, and M. Selvaggi (DELPHES 3 Collaboration), DELPHES 3, A modular framework for fast simulation of a generic collider experiment, J. High Energy Phys. 02 (2014) 057.
[79] V. Khachatryan *et al.* (CMS Collaboration), Performance of electron reconstruction and selection with the CMS detector in proton-proton collisions at $\sqrt{S} = 8$ TeV, J. Instrum. **10**, P06005 (2015).
[80] M. Aaboud *et al.* (ATLAS Collaboration), Electron efficiency measurements with the ATLAS detector using 2012 LHC proton-proton collision data, Eur. Phys. J. C **77**, 195 (2017).
[81] A. M. Sirunyan *et al.* (CMS Collaboration), Performance of the CMS muon detector and muon reconstruction with proton-proton collisions at $\sqrt{s} = 13$ TeV, J. Instrum. **13**, P06015 (2018).
[82] G. Aad *et al.* (ATLAS Collaboration), Muon reconstruction performance of the ATLAS detector in proton-proton collision data at $\sqrt{s} = 13$ TeV, Eur. Phys. J. C **76**, 292 (2016).
[83] M. Low and L.-T. Wang, Neutralino dark matter at 14 TeV and 100 TeV, J. High Energy Phys. 08 (2014) 161.
[84] V. Khachatryan *et al.* (CMS Collaboration), Measurement of the $t\bar{t}$ production cross section in the $e\mu$ channel in proton-proton collisions at $\sqrt{s} = 7$ and 8 TeV, J. High Energy Phys. 08 (2016) 029.
[85] M. Aaboud *et al.* (ATLAS Collaboration), Measurement of the $t\bar{t}$ production cross-section using $e\mu$ events with b-tagged jets in pp collisions at $\sqrt{s} = 13$ TeV with the ATLAS detector, Phys. Lett. B **761**, 136 (2016); Erratum, Phys. Lett. B **772**, 879(E) (2017).
[86] J. Alwall *et al.*, Comparative study of various algorithms for the merging of parton showers and matrix elements in hadronic collisions, Eur. Phys. J. C **53**, 473 (2008).